

1           **Functionality-Based Formation of Secondary Organic Aerosol from *m*-Xylene**  
2                                       **Photooxidation**

3           Yixin Li<sup>1,2</sup>, Jiayun Zhao<sup>1</sup>, Mario Gomez-Hernandez<sup>1</sup>, Michael Lavallee<sup>3</sup>, Natalie M. Johnson<sup>4</sup>,  
4                                       and Renyi Zhang<sup>1,3\*</sup>

5           <sup>1</sup>Department of Chemistry, Texas A&M University, College Station, TX 77843, USA

6           <sup>2</sup>Department of Chemistry, University of California Irvine, Irvine, CA 92697, USA

7           <sup>3</sup>Department of Atmospheric Sciences, Texas A&M University, College Station, TX 77843,  
8                                       USA

9           <sup>4</sup>Department of Environmental & Occupational Health, School of Public Health, Texas A&M  
10                                      University, College Station, TX 77843, USA

11   **ABSTRACT.** Photooxidation of volatile organic compounds (VOCs) produces condensable  
12   oxidized organics (COOs) to yield secondary organic aerosol (SOA), but the fundamental chemical  
13   mechanism for gas-to-particle conversion remains uncertain. Here we elucidate the production of  
14   COOs and their roles in SOA and brown carbon (BrC) formation from *m*-xylene oxidation by  
15   simultaneous monitoring the evolutions of gas-phase products and aerosol properties in an  
16   environmental chamber. Four COO types with the distinct functionalities of dicarbonyls,  
17   carboxylic acids, polyhydroxy aromatics/quinones, and nitrophenols are identified from early-  
18   generation oxidation, with the yields of 25%, 37%, 5%, and 3%, respectively. SOA formation  
19   occurs via several heterogeneous processes, including interfacial interaction, ionic  
20   dissociation/acid-base reaction, and oligomerization, with the yields of  $(20 \pm 4)\%$  and  $(32 \pm 7)\%$   
21   at 10% and 70% relative humidity (RH), respectively. Chemical speciation shows the dominant  
22   presence of oligomers, nitrogen-containing organics, and carboxylates at high RH and  
23   carboxylates at low RH. The identified BrC includes N-heterocycles/N-heterochains and

24 nitrophenols, as evident from reduced single scattering albedo. The measured uptake coefficient  
25 ( $\gamma$ ) for COOs is dependent on the functionality, ranging from  $3.7 \times 10^{-4}$  to  $1.3 \times 10^{-2}$ . A  
26 functionality-based kinetic framework is developed to predict SOA production from the  
27 measurements of the concentrations and uptake coefficients for COOs, which well reproduces  
28 SOA formation from *m*-xylene oxidation. Our results reveal that photochemical oxidation of *m*-  
29 xylene represents a major source for SOA and BrC formation under urban environments, because  
30 of its large abundance, high reactivity with OH, and high yields for COOs.

31 **Corresponding to:** Email: [renyi-zhang@tamu.edu](mailto:renyi-zhang@tamu.edu)

32

### 33 **1. Introduction**

34 Photooxidation of anthropogenic and biogenic volatile organic compounds (VOCs)  
35 produces tropospheric ozone, secondary organic aerosol (SOA), and brown carbon (BrC), with  
36 profound implications for air quality, human health, and climate (Pope et al., 2002; Li et al., 2007;  
37 IPCC, 2013; NASEM, 2016; Molina, 2021; Zhang et al., 2021). For example, SOA contributes to  
38 the Earth energy budget, directly by scattering solar radiation and indirectly by serving as cloud  
39 condensation nuclei to influence cloud formation and precipitation (IPCC, 2013; Wang et al., 2014;  
40 Zhu et al., 2017). Also, light absorbing BrC interferes with solar radiation transfer, contributing to  
41 positive radiative forcing (Wang et al. 2013; NASEM, 2016). VOC oxidation is initiated by various  
42 oxidants (e.g., OH, O<sub>3</sub>, NO<sub>3</sub>, etc.) and proceeds via multiple pathways and stages (Atkinson, 2000;  
43 Suh et al., 2001; Zhang et al., 2002; Zhao et al., 2004; Wennberg et al., 2018), yielding condensable  
44 oxidized organics (COOs) to form SOA and BrC via gas-to-particle conversion (Finlayson-Pitts  
45 and Pitts, 2000; Moise et al., 2015; Seinfeld and Pandis, 2016). Currently, the enormous chemical  
46 complexity for VOC oxidation and gas-to-particle conversion represents one of the greatest  
47 challenges in atmospheric chemistry research (Ravishankara, 1997; Zhang et al., 2015; NASEM,

48 2016). Aromatic hydrocarbons (e.g., benzene, toluene, xylenes, and trimethylbenzene) account for  
49 20-30% of the total VOCs and are the major anthropogenic SOA precursors in the urban  
50 atmosphere (Calvert et al., 2002; Ng et al., 2007; Song et al., 2007; Guo et al., 2014; Seinfeld and  
51 Pandis, 2016). For example, *m*-xylene or  $C_6H_4(CH_3)_2$  represents an important type of aromatic  
52 hydrocarbons, which is emitted primarily from industrial and traffic sources. The concentration of  
53 *m*-xylene ranges in a level from sub part per billion (ppb) up to several tens of ppb under urban  
54 environments (Calvert et al., 2002; Fortner et al., 2009). Photooxidation of *m*-xylene is primarily  
55 initiated by OH with a rate constant of  $2.4 \times 10^{-11} \text{ cm}^3 \text{ molecule}^{-1} \text{ s}^{-1}$ , which is nearly four times  
56 higher than that of toluene (Fan and Zhang, 2008; Ji et al., 2017). A laboratory study identified *m*-  
57 tolualdehyde, *m*-dimethylphenols, and dicarbonyls (i.e., glyoxal, methylglyoxal, unsaturated  
58 dicarbonyls, and epoxy carbonyls) as the main gas-phase products from OH-initiated oxidation of  
59 *m*-xylene (Zhao et al., 2005).

60         Several types of COOs with distinct functionality and volatility are produced from *m*-  
61 xylene photooxidation, contributing to aerosol nucleation and grow (Zhang et al., 2004; Zhang et  
62 al., 2015; Guo et al., 2020). SOA formation is conventionally considered to be mainly resulted  
63 from equilibrium gas-particle partitioning of semi-, intermediate-, or low-volatile products  
64 (Shrivastava et al., 2017). Aromatic oxidation by OH yields low-volatile polyhydroxy  
65 aromatics/quinones (denoted as PAQ hereafter), which condense to the aerosol-phase (Schwantes  
66 et al., 2017). Also, chain autoxidation reactions of  $RO_2$  from aromatics photooxidation likely yield  
67 highly oxygenated molecules (HOMs) with low volatility (Molteni et al., 2018; Garmash et al.,  
68 2020; Wang et al., 2020), although the reported yield of HOMs from *m*-xylene oxidation is small  
69 (1.0-1.7%) (Molteni et al., 2018). Several key oxidation products of aromatic oxidation have been  
70 shown to readily engage in multiphase reactions and contribute to SOA formation (Ji et al., 2020,

71 Li et al., 2021a). A recent experimental study demonstrated that SOA formation from toluene  
72 photooxidation is mainly contributed by volatile dicarbonyls and organic acids (Li et al., 2021b).  
73 Moreover, the aqueous reactions between small  $\alpha$ -dicarbonyls and base species (e.g., ammonia  
74 and amines) produce light-absorbing brown carbon (BrC) (De Haan et al., 2011, 2017; Marrero-  
75 Ortiz et al., 2019; Li et al., 2021a,b). Previous experimental studies identified the presence of  
76 hydroxy (C-OH), carbonyl (C=O), and acetal (C-O-C) functional groups in aromatic-derived SOA  
77 formed via aqueous reactions, implicating a role of oxygenated organics in SOA formation (Jia  
78 and Xu, 2014; Jia and Xu, 2018; Zhang et al., 2019). Also, laboratory experiments showed that  
79 coating of *m*-xylene SOA on black carbon particles significantly enhances scattering, absorption,  
80 and single scattering albedo (SSA) (Guo et al., 2016).

81 Current atmospheric models mainly parameterize SOA formation based on equilibrium  
82 partitioning for semi- to low-volatile COOs (Shrivastava et al., 2017). However, gas-to-particle  
83 conversion corresponds to decreasing entropy (i.e.,  $\Delta S \ll 0$ ), representing non-equilibrium  
84 chemical processes (Peng et al., 2021). Moreover, the occurrence of particle-phase reactions  
85 significantly alters the physiochemical properties (including volatility, hygroscopicity, and optical  
86 properties) for COOs (Tan et al., 2012; Faust et al., 2017; Ji et al., 2020; Li et al., 2021a,b; Liu et  
87 al., 2021). Notably, the volatility-based approach consistently under-predicts SOA formation  
88 (Heald et al., 2005; Zhang et al., 2015; Hodzic et al., 2016), particularly during haze formation  
89 under polluted conditions (Guo et al., 2014; Peng et al., 2021). Here we investigate the production  
90 of COOs with different functionalities and assess their roles in SOA formation from *m*-xylene  
91 oxidation. A primary objective of this work is to establish a functionality-based framework to  
92 predict SOA formation from VOC photooxidation.

## 93 2. Experimental Methodology

## 94 2.1 Chamber experiments

95 The production of COOs and their roles in SOA formation from *m*-xylene oxidation were  
96 investigated using a 1 m<sup>3</sup> chamber (Teflon® PFA, Fig. S1 in the Supplementary Information or  
97 SI), similar to our previous studies (Li et al., 2021a,b). The environmental chamber was equipped  
98 with eighteen black light lamps (18 × 30W, F30T8/350BL, Sylvania). A water bubbler at a  
99 temperature of 30°C was used to humidify the chamber to 10%, 30%, 50%, or 70% relative  
100 humidity (RH), and all experiments were performed at 298 K. Three types of seed particles were  
101 produced using a constant output atomizer (Model 3076, TSI) to represent various chemical  
102 compositions, i.e., NH<sub>4</sub>HSO<sub>4</sub> - ammonium bisulfate (ABS), (NH<sub>4</sub>)<sub>2</sub>SO<sub>4</sub> - ammonium sulfate (AS)  
103 in the presence and absence of NH<sub>3</sub>, and NaCl - sodium chloride. Seed particles were dried to RH  
104 of ~2% by a Nafion drier (PD-070–18T-12SS, Perma Pure) and size-selected for an initial size of  
105 100 nm by a differential mobility analyzer (DMA, Model 3081, TSI). Size-selected particles were  
106 injected into the chamber with an initial particle concentration of 1.5 × 10<sup>4</sup> cm<sup>-3</sup> measured by a  
107 condensation particle counter (CPC, Model 3760A, TSI). The acidity of seed particles was  
108 estimated using a thermodynamic model (Fountoukis and Nenes, 2007; Wang et al., 2018), with  
109 the pH value of 3~5 in the presence of gaseous NH<sub>3</sub> and 0~1 in the absence of gaseous NH<sub>3</sub> for  
110 (NH<sub>4</sub>)<sub>2</sub>SO<sub>4</sub>, -0.5 for NH<sub>4</sub>HSO<sub>4</sub>, and 7 for NaCl. To investigate the effects of NH<sub>3</sub> and NO<sub>x</sub>,  
111 commercially available gaseous NH<sub>3</sub> (2000 ppm NH<sub>3</sub> in N<sub>2</sub>) and NO<sub>2</sub> (500 ppm NO<sub>2</sub> in air) was  
112 injected into the chamber with a flow of 100 sccm. 600 μL H<sub>2</sub>O<sub>2</sub> (35 wt%, Sigma-Aldrich) and 10  
113 μL *m*-xylene (99.5%, Sigma-Aldrich) were injected into a glass reservoir, which was then flushed  
114 into the chamber by a 10 slpm flow from a pure air generator (Aadco 737-11, Aadco Inc.) for 10  
115 min. The gases were then mixed by a fan inside the chamber. Once desired concentrations were  
116 established, the black light lamps were turned on to initiate H<sub>2</sub>O<sub>2</sub> photolysis to generate OH

117 radicals. The initial concentration for *m*-xylene and the steady-state concentration for OH were  
118 estimated to be 1.9 ppm and  $2.1 \times 10^6$  molecules  $\text{cm}^{-3}$ , respectively (Fig. 1a). The experimental  
119 conditions are summarized in Table 1.

## 120 2.2 Analytical instruments

121 The particle size growth, density, light scattering/absorption were simultaneously and  
122 continuously monitored, after monodispersed seed particles were exposed to the products of *m*-  
123 xylene-OH oxidation in the reaction chamber. A scanning mobility particle sizer (SMPS)  
124 consisting of a DMA and a CPC was used to continuously measure the particle size growth factor,  
125  $GF = D_p/D_0$ , where  $D_p$  is the diameter after exposure and  $D_0 = 100$  nm is the initial diameter. Note  
126 both  $D_p$  and  $D_0$  correspond to the dry particle diameter measured after passing through a Nafion  
127 dryer ( $\sim 2\%$  RH). An aerosol particle mass analyzer (APM, Model 3600, Kanomax) was used to  
128 derive the particle density throughout the experiments (Li et al., 2021b). The density for the SOA  
129 materials ( $\rho_{SOA}$ ) is calculated by,

$$\rho_{SOA} = \frac{\rho \times GF^3 - \rho_0}{GF^3 - 1} \quad (1)$$

130 where  $\rho$  and GF are measured particle density ( $\text{g cm}^{-3}$ ) and growth factor at  $t$  (min), respectively.  
131  $\rho_0$  is the initial density of seed particles. The uncertainty in the density measurements was  
132 estimated to be  $\pm 0.03$   $\text{g cm}^{-3}$ .

133 To measure the optical properties of exposed particles, a 1-slp flow from the chamber  
134 was diluted by 4-slp  $\text{N}_2$  and introduced into a commercial integrating nephelometer (TSI 3563)  
135 and a home-built cavity ring-down spectrometer (CRDS) throughout the experiment. Light  
136 scattering ( $b_{\text{sca}}$ ) and extinction ( $b_{\text{ext}}$ ) at 532 nm were determined by the nephelometer and CRDS,  
137 respectively. The nephelometer was calibrated by comparing measured  $b_{\text{sca}}$  with  $b_{\text{ext}}$  from CRDS  
138 when measuring ammonium sulfate particles with diameters of 100 nm, 150 nm, 200 nm, 250 nm,

139 and 300 nm. The absorption coefficient ( $b_{\text{abs}}$ ) was determined from ( $b_{\text{ext}} - b_{\text{sca}}$ ), and SSA was  
140 calculated from  $b_{\text{sca}}/b_{\text{ext}}$ .

141 The ID-CIMS using the hydronium reagent ion ( $\text{H}_3\text{O}^+$ ) was employed to analyze gaseous  
142 concentrations with a sample flow rate of 0.5 slpm from the chamber. The sample line was heated  
143 to 70°C to reduce wall loss. Gas-phase concentrations of *m*-xylene and its oxidation products were  
144 quantified by ID-CIMS. Briefly, the concentration of species A from the proton transfer reaction  
145 ( $\text{H}_3\text{O}^+ + \text{A} \rightarrow \text{H}_2\text{O} + \text{HA}^+$ ) is determined by,

$$[\text{A}] = \frac{S_{\text{A}}}{k_{\text{PTR}} \times \Delta t \times S_{\text{RI}}} \quad (2)$$

146 where  $S_{\text{A}}$  and  $S_{\text{RI}}$  are the mass spectrum intensities for A and reagent ions, respectively.  $k_{\text{PTR}}$  is the  
147 proton-transfer rate constant between A and  $\text{H}_3\text{O}^+$  (Zhao and Zhang, 2004).  $\Delta t = \frac{l}{U_i}$  is the retention  
148 time of ions, which is determined by the length of the drift tube  $l = 8$  cm and the ion drift velocity  
149  $U_i$ . The ion drift velocity  $U_i$  is determined from:

$$U_i = u_0 \left( \frac{760 \text{ torr}}{p} \right) \left( \frac{T}{273 \text{ K}} \right) E \quad (3)$$

150 where  $u_0 = 2 \text{ cm}^2 \text{ V}^{-1} \text{ s}^{-1}$  is the reduced ionic mobility (Dotan et al., 1976),  $p = 3.0$  torr,  $T = 298$  K,  
151 and  $E = 133 \text{ V cm}^{-1}$  is the voltage gradient in the drift tube. Alternatively, the concentrations of *m*-  
152 xylene, dicarbonyls, and organic acids were also calibrated by preparing the vapors of *m*-xylene,  
153 methylglyoxal with known mixing ratios in  $\text{N}_2$ , and using a permeation tube of propanoic acid,  
154 respectively (Li et al., 2021a). The detection limit (defined as 3 times of the ratio of signal to noise)  
155 for the oxidation products from *m*-xylene-OH reactions was estimated to be 50 ppt by the ID-  
156 CIMS.

157 The steady-state OH concentration was determined by exponential fitting ( $y = ke^{-bx}$ ) of  
158 the decay of *m*-xylene concentration (Fig. 1a),

$$[\text{OH}] = \frac{b}{k_1} \quad (4)$$

159 where  $k_1 = 2.4 \times 10^{-11} \text{ cm}^3 \text{ molecule}^{-1} \text{ s}^{-1}$  is the second-order rate constant for *m*-xylene-OH  
 160 oxidation (Fan and Zhang, 2008). The estimated concentration of OH was  $2.1 \times 10^6 \text{ molecules cm}^{-3}$   
 161 <sup>3</sup> in our experiments.

162 We also estimated loss of condensable vapors to the chamber wall using the first-order  
 163 wall-loss coefficient,  $k_w \text{ (s}^{-1}\text{)}$ , by considering gas-phase transport within the chamber (Zhang et  
 164 al., 2014)

$$k_w = \left(\frac{A}{V}\right) \frac{\alpha_w \bar{c}}{4 + \frac{\pi}{2} \left(\frac{\alpha_w \bar{c}}{\sqrt{k_e D_g}}\right)} \quad (5)$$

165 where  $A/V$  is the surface to volume ratio of the chamber (equal to  $6/L$  for a square chamber, where  
 166  $L = 1 \text{ m}$  is its dimension),  $\alpha_w$  is the mass accommodation coefficient of vapors onto Teflon chamber  
 167 walls,  $\bar{c}$  is the mean thermal speed of the molecules,  $k_e$  is the coefficient of eddy diffusion, which  
 168 is estimated to be 0.5 based on the loss rate of particles (McMurry and Rader, 1985),

$$k_e = \frac{\left(\frac{\pi L \beta_0}{12}\right)^2}{D_b} \quad (6)$$

169 where  $\beta_0$  is the fractional loss rate of particles,

$$\beta_0 = \frac{\Delta N}{N \times \Delta t} = \frac{15000 \text{ cm}^{-3} - 7500 \text{ cm}^{-3}}{15000 \text{ cm}^{-3} \times 7200 \text{ s}} = 1.4 \times 10^{-5} \text{ s}^{-1} \quad (7)$$

170 where  $N$  is the particle number concentration,  $D_b = 6.75 \times 10^{-10} \text{ m}^2 \text{ s}^{-1}$  is the Brownian diffusion  
 171 coefficient for particles.  $D_g$  is the gas-phase diffusion coefficient. For  $\text{NH}_3$ , the mass  
 172 accommodation coefficient of vapors onto the chamber wall is 0.05 (Zhang et al., 2014). Gas-  
 173 phase diffusion constant  $D_g$  is  $1.98 \times 10^{-5} \text{ m}^2 \text{ s}^{-1}$ . The mean thermal speed  $\bar{c}$  is  $603 \text{ m s}^{-1}$ . The first-  
 174 order wall-loss coefficient of  $\text{NH}_3$  was calculated to be  $1.2 \times 10^{-2} \text{ s}^{-1}$ .



175 The average concentration of NH<sub>3</sub> or NO<sub>x</sub> (noted as X) is estimated by,

$$\overline{[X]} = \frac{(1 - e^{-k_w \times \Delta t_i})}{k_w \times \Delta t_i} [X]_0 \quad (8)$$

176 For initial injection of 400 ppb NH<sub>3</sub>, the average concentration of NH<sub>3</sub> was estimated to be 19 ppb.

177 The first-order wall-loss rate of NO<sub>x</sub> was measured to be  $2.5 \times 10^{-3} \text{ h}^{-1}$ , leading to negligible wall-

178 loss (Qi et al., 2020).

179 The particle-phase chemical composition was analyzed by thermal desorption (TD) - ID -  
180 CIMS (TD-ID-CIMS) (Wang et al., 2010). Seed particles after 20 min of exposure to  
181 photooxidation were collected for 2 hours by a platinum filament (with a collection voltage of  
182 about 3000 V) in a 2.5 slpm flow from the reaction chamber, and the analytes were evaporated by  
183 heating the filament to 350°C for 2 s and detected by ID-CIMS using H<sub>3</sub>O<sup>+</sup> as the reagent ions.  
184 The mass resolution of TD-ID-CIMS was about 0.5 amu. The desorption signal was represented  
185 by the relative intensity (RI) of the integrated peak area during heating. The uncertainties of TD-  
186 ID-CIMS measurements arose from the flow rate, voltage, collection time, evaporation voltage,  
187 and mass spectrometer ionization/detection efficiencies during particle collection and were  
188 represented by the standard deviation of three repeated measurements. In both ID-CIMS and TD-  
189 ID-CIMS configurations, an ion drift-tube was used. An electric field of E/N = 138 Td was applied  
190 for ID-CIMS at high RH (i.e., 70%), and E/N = 110 Td was used for TD-ID-CIMS at low RH (<  
191 1%). Formation of cluster ions was effectively suppressed, since a uniform electrical field in the  
192 drift tube decomposed weakly-bonded cluster ions. Fragmentation using ID-CIMS or TD-ID-  
193 CIMS was minimal, and all gaseous and particle-phase products were detected at their respective  
194 parent-peaks, indicating little dissociation effect from either thermal desorption or ionization by  
195 H<sub>3</sub>O<sup>+</sup> (Yuan et al., 2017). For example, plausible fragment-ion peaks for oligomers and organic  
196 acids are the monomeric ion-peaks and [M-17]<sup>+</sup>/[M-45]<sup>+</sup> from α-cleavage, respectively. From our

197 detected particle-phase products (Fig. 2c), non-fragmental oligomers/NCO and organic acids  
198 represented the dominant peaks, while negligible monomer (e.g.,  $m/z = 73$ ) and fragments for  
199 organic acids (e.g., [M-17] or [M-45]) were detected, confirming little fragmentation by TD-ID-  
200 CIMS measurement. Also, the major acetal/hemiacetal oligomers detected by TD-ID-CIMS at  
201 high RH from *m*-xylene oxidation were consistent with a previous study showing intact oligomers  
202 with thermal desorption (Claflin and Ziemann, 2019).

203 While the gaseous concentrations of the oxidation products, GF, SSA, and density were  
204 temporally resolved in our experiments, the particle chemical composition reflected an overall  
205 aerosol chemical makeup during an experiment. To assess the effects of different seed particles,  
206 RH, and NH<sub>3</sub> on SOA and BrC formation, we compared the measured GF and SSA values after  
207 120-min exposure to the *m*-xylene-OH oxidation.

### 208 2.3 Uptake coefficient ( $\gamma$ ) determination

209 The uptake coefficient ( $\gamma$ ) for COOs is calculated by,

$$\gamma = \frac{4 \times FR \times kp}{\bar{c} \times S} \quad (9)$$

210 where  $FR$  is the percent contributions of the COO species from *m*-xylene-OH oxidation to the  
211 particle-phase mass intensity measured by TD-ID-CIMS.  $kp$  is measured first-order particle uptake  
212 rate constant for COOs (i.e., glyoxal, methylglyoxal,  $\gamma$ -dicarbonyls, organic acids, PAQ, and  
213 nitrophenols), which is calculated from the measured growth rate of seed particles,

$$kp = \frac{\pi \times (D_p^3 - D_0^3) \times \rho \times \bar{N} \times N_A}{6 \times MW \times [A] \times \Delta t} \quad (10)$$

214 where  $D_p$  and  $D_0$  are the final and initial diameters of the particles during the time-period of 120  
215 min, respectively,  $\rho$  is the density of total SOA,  $\bar{N} = 11250 \text{ cm}^{-3}$  is the average particle number  
216 concentration during 120 min,  $\Delta t = 120 \text{ min}$  is the exposure time,  $N_A$  is Avogadro constant, MW

217 is the molar weight of species A, and  $[A]$  is the average gas phase concentration of species A.  $\bar{c}$  is  
 218 the mean thermal speed of A.  $S$  is the average surface area of aerosols ( $\text{cm}^2 \text{ surface}/\text{cm}^3 \text{ air}$ ) during  
 219 the period of  $\Delta t = 120 \text{ min}$ ,

$$S = \frac{\pi \int_{t=0}^{120 \text{ min}} D^2 \times HGf^2 \times \bar{N} dt}{\Delta t} \quad (11)$$

220 where  $D$  is the time-dependent particle diameter,  $HGf$  is the hygroscopic growth factor of particles  
 221 (Seinfeld and Pandis, 2016). The error bars of reactive coefficients are derived from the  
 222 propagation of uncertainties for the parameters in eqs. 9-11 (i.e.,  $1 \sigma$  of at least three repeated  
 223 measurements for each parameter).

#### 224 **2.4 Simulation of gaseous oxidation products**

225 The gas-phase concentration of *m*-xylene-OH oxidation products were simulated by a tri-  
 226 exponential kinetic model to account for the gas-phase oxidation, chamber wall loss, and particle  
 227 uptake. The precursor A with an initial concentration of  $[A]_0$  undergoes multiple steps of oxidation  
 228 to yield multi-generation products,  $P_n$  (where  $n = 1, 2, 3, \dots$ ). Once formed, each product engages  
 229 in further oxidation with a pseudo first-order rate constant of  $k'_{n+1} = k_{n+1}[\text{OH}]_{\text{ss}}$ , particle uptake  
 230 with a rate constant of  $kp_n$ , and wall loss with a rate of  $kw_n$ . The forward rate constants,  $k_{n+1}$ , were  
 231 taken from MCM 3.3.1 (Jenkin et al., 2003). The rate constant of uptake  $kp_n$  is expressed by,

$$kp_n = \frac{1}{4} \gamma_n \bar{c} S \quad (12)$$

232 and the first-order wall loss rate constants were estimated by eq. 5 with the mass accommodation  
 233 coefficients  $\alpha_w$  constrained by the measured time-dependent concentration. The gas-phase  
 234 concentrations of  $P_1$  to  $P_3$  are calculated by,

$$[P_1] = \frac{k'_1 [A]_0}{k'_2 + kw_1 + kp_1 - k'_1} (e^{-k'_1 t} - e^{-(k'_2 + kw_1 + kp_1)t}) \quad (13)$$

$$[P_2] = C_1 e^{-(k'_3 + kw_2 + kp_2)t} + C_2 e^{-k'_1 t} - C_3 e^{-(k'_2 + kw_1 + kp_1)t} \quad (14)$$

$$[P_3] = C_4 e^{-(k'_4 + kw_3 + kp_3)t} + C_5 e^{-(k'_3 + kw_2 + kp_2)t} + C_6 e^{-k'_1 t} - C_7 e^{-(k'_2 + kw_1 + kp_1)t} \quad (15)$$

235 where  $C_1$  to  $C_7$  are constants, and  $k'_n$  denotes the pseudo-first order rate constant,

$$k'_n = k_n[\text{OH}] \quad (16)$$

236 The rate constants and values for  $C_1$  to  $C_7$  are summarized in Table S1.

## 237 **2.5 COO yield**

238 The COO yield ( $Y_{\text{COO}}$ ) from *m*-xylene oxidation is determined from,

$$239 \quad Y_{\text{COO}} = [\text{COO}_i] / \Delta[\text{C}_6\text{H}_4(\text{CH}_3)_2] \quad (17)$$

240 where  $i$  represents the type of COO species, and  $\Delta[\text{C}_6\text{H}_4(\text{CH}_3)_2]$  denotes the concentration of *m*-  
 241 xylene consumed due to OH oxidation. There were four types of COOs identified from our  
 242 experiments, i.e., dicarbonyls for  $i = 1$ , carboxylic acids for  $i = 2$ , PAQ for  $i = 3$ , and nitrophenols  
 243 for  $i = 4$ . The measured gaseous concentration for each COO is corrected for wall-loss and  
 244 unreacted earlier generation products,

$$[\text{COO}_i] = \left\{ [\text{COO}_{i,f}] + \left( \frac{1}{4} \gamma_i \bar{c} S + kw_i \right) \overline{[\text{COO}_i]} \Delta t \right\} / \left( 1 - \frac{[A_f]}{[A_t]} \right) \quad (18)$$

245 where  $[\text{COO}_{i,f}]$  and  $\overline{[\text{COO}_i]}$  are the final and time-averaged gas-phase concentrations of  $\text{COO}_i$  at  
 246 120 min, respectively.  $[A_f]$  and  $[A_t]$  are the unreacted and the total production of the earlier  
 247 generation species A, respectively.

## 248 **2.6 SOA mass concentration and yield**

249 The measured SOA mass concentration is calculated based on the aerosol size growth and  
 250 density,

$$M_{\text{SOA,meas.}} = \frac{1}{6} \pi (D_p^3 \times \rho_t - D_0^3 \times \rho_0) \times \bar{N} \quad (19)$$

251 where  $\rho_t$  and  $\rho_0$  are the final and initial particle density during 120 min, respectively.  
 252 Alternatively, by categorizing COOs in accordance with the functional groups, we established a  
 253 framework to predict SOA formation from the measured production and reactivity. The SOA mass  
 254 concentration ( $M_{SOA}$ ) is predicted from the measured uptake coefficients and average gas-phase  
 255 concentrations of COOs,

$$M_{SOA} = \sum_i^4 \frac{1}{4} \gamma_i \bar{c}_i S [A_i] MW_i \quad (20)$$

256 where  $MW_i$  is the molar weight of species  $i$ .  $\gamma_i$  is averaged over all identified species for each type  
 257 ( $i$ ) of COOs, and  $[A_i]$  is the sum of the measured concentrations of all identified species for type  $i$   
 258 (time-averaged). The SOA mass yield is expressed by,

$$Y_{SOA} = M_{SOA} / \{ \Delta [C_6H_4(CH_3)_2] \times MW_m \} \quad (21)$$

260 where  $MW_m$  is the molar weight of *m*-xylene.

261 To compare the measured and predicted SOA formation at RH = 10% and 70%, we  
 262 corrected the increased vapor wall loss and reduced particle surface area at RH = 70% compared  
 263 to 10% RH. A correction factor is determined from the average measured gas concentration ratios  
 264 ( $R_c$ ) between 10% and 70% RH for each type of COOs. Additionally, a hygroscopic volume  
 265 enhancement factor (HVE) of 1.2 between 10% and 70% RH is adopted. The RH-corrected SOA  
 266 mass for each COO is estimated by,

$$M_{i,corr} = R_c \times M_{SOA} \times \frac{S_1}{S_2} \times HVE \quad (22)$$

267 where  $S_1$  and  $S_2$  are the particle surface areas at 10% and 70% RH, respectively.

## 268 3. Results and Discussions

### 269 3.1 Evolution of oxidation products

270 To elucidate the production of COOs, we measured time-dependent gaseous concentrations  
271 of *m*-xylene oxidation products. The OH-*m*-xylene reactions occur via dominantly OH-addition to  
272 the aromatic ring to yield *m*-xylene-OH adducts and minorly H-abstraction from the methyl group  
273 to form methylbenzyl radicals (about 4%) (Fan and Zhang, 2008). The *m*-xylene-OH adducts then  
274 react with O<sub>2</sub> to form dimethylphenol via H-extraction or OH-*m*-xylene-O<sub>2</sub> peroxy radicals (RO<sub>2</sub>)  
275 via O<sub>2</sub> addition (Fig. S2a). While the *m*-xylene mixing ratio exhibits an exponential decay  
276 throughout the experiments (Fig. 1a), the formation of the gas-phase oxidation products follows  
277 the rate-determining steps involving successive OH-oxidation with three major generations (Fig.  
278 1b-e). The first-generation products (P<sub>1</sub>) include dimethylphenol ( $m/z = 123$ ) and  
279 methylbenzaldehyde ( $m/z = 121$ ), corresponding to OH addition to the aromatic ring (~96%) and  
280 hydrogen extraction (~4%) from the methyl group, respectively (Fan and Zhang, 2008; Li et al.,  
281 2021b). The second-generation products (P<sub>2</sub>) mainly consist of methylglyoxal ( $m/z = 73$ ),  
282 methylbutenedial ( $m/z = 99$ ), toluic acid ( $m/z = 137$ ), and dimethylresorcinol (Fig. 1f and Fig. S2b),  
283 which are produced from the P<sub>1</sub> reactions with OH/HO<sub>2</sub>. For example, methylglyoxal and  
284 methylbutenedial are formed from OH oxidation of dimethylphenol and subsequent ring-  
285 opening or from the primary peroxy radical. The latter undergoes cyclization to form the bicyclic  
286 radical, which then reacts with O<sub>2</sub> to form the secondary peroxy radical, followed by reactions  
287 with HO<sub>2</sub> and subsequent ring-cleavage (Fan and Zhang, 2008). The third-generation products (P<sub>3</sub>)  
288 contain mainly multi-functional organic acids, including pyruvic acid ( $m/z = 89$ ), 4-oxo-2-  
289 pentenoic acid ( $m/z = 115$ ), and 3-methyl-4-oxo-2-pentenoic acid ( $m/z = 129$ ) produced from the  
290 subsequent reactions of dicarbonyls with OH. Note that P<sub>n</sub> in Fig. 1b denotes the lumped product  
291 of the  $n^{\text{th}}$  generation, which is related the sequence of OH addition for *m*-xylene oxidation and  
292 accounts for the various species detected by ID-CIMS (Fig. S2b).

293           The P<sub>1</sub> concentrations rise immediately upon initiating photooxidation and reach the peak  
294 mixing ratios of about 20 ppb for dimethylphenol and 9 ppb for methylbenzaldehyde. There is a  
295 slight decline in P<sub>1</sub> concentrations after 70 to 100 mins, reflecting their consumption from further  
296 OH oxidation (Fig. 1c). The P<sub>2</sub> concentrations follow those of P<sub>1</sub> (Fig. 1d and Fig. S3a) and reach  
297 the peak mixing ratios ranging from 0.4 to 2.4 ppb, dependent on their subsequent oxidation by  
298 OH as well as loss to the chamber wall and aerosols. Note that the concentration of toluic acid  
299 rises later than those of the dicarbonyls, attributable to the slower rates for H-abstraction by OH  
300 from the methyl group than OH-addition to the aromatic ring (Fan and Zhang, 2008). The P<sub>3</sub>  
301 concentrations increase monotonically after a delay of 10-20 mins and reach a mixing ratio from  
302 sub-ppb to 2.5 ppb at 120 min (Fig. 1e and Fig. S3b). The initial concentration of *m*-xylene (e.g.,  
303 1940 ppb) in our experiment is higher than that in the atmosphere, potentially inducing self- and  
304 cross-reactions of RO<sub>2</sub> to form alkoxy radicals (RO) or dialkyl peroxides (ROOR') leading to  
305 HOMs. However, negligible products relevant to HOMs were detected in our experiments,  
306 indicating a minor importance for the self- and cross-reactions of RO<sub>2</sub> compared to the competing  
307 reactions between RO<sub>2</sub> and HO<sub>2</sub>/NO/RO<sub>2</sub> to form ring-opening products. Our results for  
308 insignificant contribution of HOMs to SOA formation from *m*-xylene oxidation are consistent with  
309 a small yield of HOMs reported in a previous study (Molteni et al., 2018).

310           We simulated the time-dependent evolution of the gaseous products by employing a tri-  
311 exponential kinetic model (Fig. 1b and Table S1). Multi-generation oxidation of *m*-xylene occurs  
312 via consecutive reaction steps to produce a multi-generation product, P<sub>*n*</sub> (where *n* denotes the  
313 sequence of OH oxidation), which subsequently engages in additional OH oxidation, wall loss,  
314 and aerosol loss. Fig. 1b-d indicates that the simulated concentrations well reproduce those

315 measured for P<sub>1</sub> to P<sub>3</sub> by adopting our measured  $\gamma$  (to be discussed below) and estimated wall loss  
316 rates (see Methods and Table S1 in SI).

### 317 **3.2 Particle size growth, SSA, and chemical speciation**

318 To evaluate SOA and BrC formation from COOs, we measured the time-dependent GF,  
319 SSA, and density, after (NH<sub>4</sub>)<sub>2</sub>SO<sub>4</sub> seed particles are exposed to the *m*-xylene oxidation products  
320 in the presence of 19 ppb NH<sub>3</sub> and at 70% RH (Fig. 2a-c, Exp. 1). The GF increases monotonically  
321 and reaches a value of  $(2.41 \pm 0.03)$  at 120 min (Fig. 2a), while the SSA declines steadily  
322 throughout the exposure and reaches the value of  $(0.91 \pm 0.01)$  at 120 min (Fig. 2b). The latter is  
323 indicative of the production of light-absorbing BrC. The measured SSA for *m*-xylene is lower than  
324 that previously reported for toluene under comparable experimental conditions (Li et al., 2021b).  
325 The difference in SSA/BrC formation between toluene and *m*-xylene is explained by a higher yield  
326 of methylglyoxal from *m*-xylene than from toluene (Jenkin et al., 2003; Nishino et al., 2010), since  
327 methylglyoxal produces BrC more efficiently via aqueous reaction than glyoxal (Li et al., 2021a).  
328 Analysis of particle chemical composition using TD-ID-CIMS reveals high abundances of  
329 oligomers, nitrogen-containing organics (NCO) consisting of N-heterocycles/N-heterochains,  
330 carboxylates, along with a small amount of dimethylresorcinol/benzoquinone (Fig. 2c). The  
331 identified mass peaks are summarized in Tables S2 to S4. Assuming similar sensitivity to proton-  
332 transfer reactions for the aerosol-phase organics, i.e., with the proton transfer reaction rate  
333 constants of  $(2 \text{ to } 4) \times 10^{-9} \text{ cm}^3 \text{ molecule}^{-1} \text{ s}^{-1}$  (Zhao and Zhang, 2004), the contributions of  
334 oligomers, NCO, carboxylates, and dimethylresorcinol/benzoquinone to the total SOA formation  
335 are estimated to be 22%, 23%, 47%, and 8%, respectively, at 70% RH (Table S5). Note that the  
336 TD-ID-CIMS method preserves the identify for all organic species without fragmentation,  
337 providing unambiguous chemical speciation for the aerosol-phase products.



### 338 3.3 Effects of seed particles, NH<sub>3</sub>, RH, and NO<sub>x</sub>

339 We assessed the dependence of SOA/BrC formation from *m*-xylene-OH oxidation on  
340 different seed particles (Exp. 1-4), NH<sub>3</sub> concentration (Exp. 1-12), RH (Exp. 1,13-15), and NO<sub>x</sub>  
341 concentration (Exp. 1,16-18). Fig. 3a shows that (NH<sub>4</sub>)<sub>2</sub>SO<sub>4</sub> in the presence of 19 ppb NH<sub>3</sub> exhibits  
342 the largest GF and lowest SSA at 120 min, which are explained by the chemical mechanisms  
343 leading to the formation of the observed aerosol-phase products. While dicarbonyls undergo  
344 aqueous phase reactions to form oligomers (Fig. S4) (Ji et al., 2020; Li et al., 2021a), organic acids  
345 engage in ionic dissociation and acid-base reaction to yield carboxylates (Fig. 3b). In addition, the  
346 reaction of dicarbonyls with NH<sub>3</sub> produces N-heterocycles/N-heterochains (Fig. S5), which are  
347 light-absorbing (Marrero-Ortiz et al., 2019; Li et al., 2021a). Oligomerization of dicarbonyls  
348 involves protonation, hydration, and deprotonation, which are mediated by carbenium ions via  
349 nucleophilic addition (Ji et al., 2020; Li et al., 2021a). While protonation of dicarbonyls to yield  
350 carbenium ions is promoted by hydrogen ion activity, high acidity hinders hydration and  
351 deprotonation, explaining the largest GF and the smallest SSA on weakly acidic (NH<sub>4</sub>)<sub>2</sub>SO<sub>4</sub>  
352 particles in the presence NH<sub>3</sub> (Fig. 3a). In addition, uptake of dicarbonyls, organic acids, and PAQ  
353 is likely facilitated on aqueous (NH<sub>4</sub>)<sub>2</sub>SO<sub>4</sub> particles, because of surface propensity of charge-  
354 separation at the interface (Hua et al., 2011; Shi et al., 2020). Specifically, surface-abundant NH<sub>4</sub><sup>+</sup>  
355 cations arising from interfacial charge separation of (NH<sub>4</sub>)<sub>2</sub>SO<sub>4</sub> likely exert electrostatic attraction  
356 to gaseous oxygenated species (with a negative charge character) to enhance uptake for  
357 dicarbonyls, organic acids, and PAQ (Li et al., 2021a,b). The most efficient formation of SOA and  
358 BrC on (NH<sub>4</sub>)<sub>2</sub>SO<sub>4</sub> particles in the presence of NH<sub>3</sub> are also consistent with the measured highest  
359 intensities for oligomers and NCO (Fig. 3b). On the other hand, ionic dissociation and acid-base  
360 reaction to yield carboxylates occur efficiently in the presence of NH<sub>3</sub>/NaCl, as evident from the

361 increasing carboxylate intensity from  $\text{NH}_4\text{HSO}_4$  to  $\text{NaCl}$  (Fig. 3b). The GF and SSA increase and  
362 decrease, respectively, with  $\text{NH}_3$  from 0 to 27 ppb for all three types of seed particles (Fig. 4a,b),  
363 relevant to the reactions of  $\text{NH}_3$  with dicarbonyls to form NCO and with organic acids to form  
364 ammonium carboxylates. The analysis of the particle composition confirms that the intensities of  
365 oligomers, NCO, and carboxylates increase with the  $\text{NH}_3$  concentration (Fig. 4c-e).

366 We carried out additional experiments by varying RH from 10% to 70% in the presence of  
367 19 ppb  $\text{NH}_3$  (Fig. 5). The GF decreases with increasing RH from  $(3.10 \pm 0.06)$  at RH = 10% to  
368  $(2.41 \pm 0.03)$  at RH = 70% (Fig. 5a). The measured SSA at 120 min is close to unity at 10% and  
369 30% RH and decreases with increasing RH (Fig. 5a), indicating negligible NCO formation at low  
370 RH but significant NCO formation at RH above 50%. Carboxylates represent the dominant  
371 constituent throughout the RH range (i.e., 85% at 10% RH to 47% at 70% RH), while the  
372 contributions of oligomers and NCO are small at low RH (2-5% at RH < 40%) and become  
373 increasingly significant at high RH (15-23% at RH > 50%) (Fig. 5b). The fraction for PAQ (8%)  
374 is nearly invariant with RH. For  $(\text{NH}_4)_2\text{SO}_4$  particles, the deliquescent and efflorescent points are  
375 at 80% and 36% RH, respectively (Li et al., 2021b). At low RH (10% and 30%), aqueous reactions  
376 to yield oligomers/NCO are minimal because of small water activity and significantly suppressed  
377 protonation and oligomerization. On the other hand, carboxylic acids readily undergo ionic  
378 dissociation or acid-base reaction, since organic acids efficiently retain water even at low RH (Xue,  
379 2009). The equilibrium vapor pressures for PAQ are much lower than those for organic acids  
380 (Table S6), facilitating more efficient condensation. Additionally, wall-loss of COOs is more  
381 pronounced at high RH (Li et al., 2021b), explaining the decreased GF with increasing RH.  
382 Measurement of gaseous concentrations for COOs shows that wall-loss is 1.5 to 4.6 times more

383 efficient at 70% RH than at 10% RH, while wall loss of *m*-xylene is negligible at both RH levels  
384 (Table S7).

385 We determined the total density and the density of the SOA fraction for (NH<sub>4</sub>)<sub>2</sub>SO<sub>4</sub> seed  
386 particles exposed to *m*-xylene oxidation (Fig. 5 c,d). The measured densities are distinct between  
387 10 and 70% RH. At 10% RH, the total density decreases monotonically, while the SOA density  
388 increases slightly with reaction time, i.e., from 1.27 to 1.39 g cm<sup>-3</sup> (Fig. 5c), indicating minor  
389 oligomers and dominant carboxylic acids at low RH. At 70% RH, the total particle density initially  
390 decreases from 1.77 g cm<sup>-3</sup> to 1.41 g cm<sup>-3</sup> (at a GF of 1.24) and subsequently increases steadily to  
391 1.56 g cm<sup>-3</sup> at 120 min. The SOA density on (NH<sub>4</sub>)<sub>2</sub>SO<sub>4</sub> particles increases from 1.26 g cm<sup>-3</sup> at 10  
392 min to 1.55 g cm<sup>-3</sup> at 120 min (Fig. 5d). The evolution in the densities reflects the variation in the  
393 chemical composition. The initial particle growth is dominated by small oligomers, imidazoles  
394 from methylglyoxal/methylbutenedial, and early-generation organic acids (e.g., toluic acid), with  
395 the densities from 0.98 to 1.27 g cm<sup>-3</sup> (Table S8). Subsequent particle growth from  
396 methylglyoxal/methylbutenedial yields large oligomers, with the densities of 1.71-1.90 g cm<sup>-3</sup>  
397 (Table S8).

398 To evaluate the NO<sub>x</sub> effects, we performed experiments on (NH<sub>4</sub>)<sub>2</sub>SO<sub>4</sub> seed particles by  
399 varying the initial NO<sub>x</sub> concentration from 0 to 500 ppb (Fig. 6). Three major nitrophenols are  
400 identified from NO<sub>2</sub> addition to the OH-*m*-xylene adduct, i.e., 4-methyl-2-nitrophenol (*m/z* = 154),  
401 dimethyl nitrophenol (*m/z* = 168), and dimethyl-4-nitrocatechol (*m/z* = 184) (Fig. 6a). The  
402 production of nitrophenols is much smaller than those for dicarbonyls and organic acids, consistent  
403 with a smaller yield (less than 7%) for nitrophenols (Fan and Zhang, 2008). The GF on (NH<sub>4</sub>)<sub>2</sub>SO<sub>4</sub>  
404 seed particles with NH<sub>3</sub> decreases from 2.41 ± 0.03 to 2.18 ± 0.03 with 0 to 500 ppb NO<sub>x</sub> (Fig. 6b).  
405 The SSA decreases significantly from 0.911 ± 0.006 to 0.839 ± 0.003 with increasing NO<sub>x</sub> (Fig.

406 6b), because of the formation of light-absorbing nitrophenols (Hems and Abbatt, 2018; Li et al.,  
407 2021b). Analysis of particle composition reveals that the decreasing GF with increasing NO<sub>x</sub>  
408 correlates with simultaneous decreases of carboxylates, oligomers, and NCOs and with increasing  
409 nitrophenols in the aerosol-phase (Fig. 6c). Overall, nitrophenols contribute 2% to 4% to the SOA  
410 formation. Addition of NO<sub>x</sub> not only produces nitrophenols and but also alters the cycling between  
411 RO<sub>2</sub> and alkoxy (RO) radicals, leading to re-distributions of COOs. The presence of NO<sub>x</sub> decreases  
412 dicarbonyls and organic acids, as evident from decreased intensities for oligomers, NCO, and  
413 carboxylates in the aerosol-phase with increasing NO<sub>x</sub> (Fig. 2h).

### 414 **3.4 COO and SOA Yields**

415 From the measured GF and COO concentrations, we derived the  $\gamma$ , which is widely  
416 employed to represent aerosol formation in atmospheric models (Zhang et al., 2015). The  
417 measured  $\gamma$  varies with the functionality of COOs and RH on (NH<sub>4</sub>)<sub>2</sub>SO<sub>4</sub> seed particles (Fig. 7a).  
418 Results of the  $\gamma$  values for COOs are also summarized in Table S9. The  $\gamma$  for dicarbonyls is the  
419 highest (from  $3 \times 10^{-3}$  to  $1.3 \times 10^{-2}$ ) at 70% RH but is significantly reduced (from  $3.7 \times 10^{-4}$  to  $1.0$   
420  $\times 10^{-3}$ ) at 10% RH, while the  $\gamma$ 's for organic acids, PAQ, and nitrophenols are slightly higher at  
421 70% RH. Among the organic acids, the  $\gamma$  correlates with the acid dissociation constant and  
422 solubility, which are the highest for pyruvic acid and the lowest for toluic acid. The standard  
423 variation in  $\gamma$  (within one  $\sigma$ ) among each COO type is within 50%, 40%, 30%, and 15% for  
424 dicarbonyls, organic acids, PAQ, and nitrophenols, respectively. From the measured  
425 concentrations of COOs and *m*-xylene, we determined the COO yields ( $Y_{\text{COO}}$ ) using eq. 17, by  
426 considering four COO species, i.e., dicarbonyls for  $i = 1$ , carboxylic acids for  $i = 2$ , PAQ for  $i = 3$ ,  
427 and nitrophenols for  $i = 4$  (Table S7). The  $Y_{\text{COO}}$  values for dicarbonyls, organic acids, PAQ, and

428 nitrophenols are 25%, 37%, 5%, and 3%, respectively (Fig. 7b), indicating significant production  
429 of COOs from *m*-xylene oxidation.

430 Our work shows significant increase in particle size (Fig. 2a) and constantly varying  
431 particle properties, i.e., SSA (Fig. 2b) and density (Fig. 5c,d), which correlate closely with the  
432 gaseous COO production (Fig. 1). These results imply a highly nonequilibrium kinetic process  
433 leading to SOA formation from *m*-xylene oxidation, which cannot be described by equilibrium  
434 partitioning. The gas-to-particle conversion from *m*-xylene oxidation is dominated by several  
435 volatile COO species (i.e., organic acids and dicarbonyls) and with minor contribution from  
436 condensation of low-volatility COO (i.e., polyhydroxy aromatics/quinones, and nitrophenols) (Fig.  
437 5b). In our study, the vapor pressures of the detected gaseous oxidation products for organic acids  
438 and dicarbonyls are too large to explain the measured particle growth via equilibrium partitioning  
439 (Table S6). Specifically, the saturation vapor pressures of organic acids detected in the particle-  
440 phase range from  $1.9 \times 10^{-3}$  to  $6.6 \times 10^{-6}$  atm, while their gas-phase concentrations range from 0.5  
441 to 2.5 ppb. Similarly, the saturation vapor pressures of dicarbonyls detected in the particle-phase  
442 range from  $1.6 \times 10^{-1}$  to  $3.9 \times 10^{-4}$  atm, while their gas-phase concentrations range from 0.5 to 2.2  
443 ppb. The high saturation vapor pressures and low gas-phase concentrations for dicarbonyls and  
444 organic acids render equilibrium partitioning implausible for these COOs in our experiments. Also,  
445 the detection of the particle-phase products confirms that organic acids and dicarbonyls directly  
446 participate in heterogeneous reactions to yield low-volatile products. Moreover, volatility-based  
447 equilibrium partitioning cannot not explain the variations in the particle size growth, SSA, and  
448 chemical compositions on different seed particles (Fig. 3). Clearly, the gas-to-particle conversion  
449 from *m*-xylene oxidation likely involves several distinct heterogeneous processes, including the

450 interfacial interaction, ionic dissociation/acid-base reaction, and nucleophilic oligomerization (Li  
451 et al., 2021a,b).

452 We establish a functionality-based SOA formation to predict the aerosol mass  
453 concentration ( $M_{SOA}$ ) from the gaseous concentrations and  $\gamma$ 's for COOs using eq. 20. The  $M_{SOA}$   
454 is calculated from the measurements of the averaged  $\gamma$  (Fig. 7a and Table S10) and the time-  
455 averaged concentrations for each COO type (Table S7). While the production of COOs is  
456 dependent on the VOC types and photooxidation, the aerosol-phase reactivity of COOs, as  
457 represented by  $\gamma$ , is dependent on the functionality for a given aerosol type. Thus, SOA formation  
458 from various VOC types can be predicted from the production and reactivity for COOs based on  
459 the experimental measurements, by categorizing COOs in accordance with their functional groups.  
460 The overall gas uptake onto liquid or solid particles is commonly described by an empirical  
461 framework on the basis of an effective  $\gamma$ , which accounts for the gas-phase diffusion, the interfacial  
462 process (i.e., accommodation), and the aerosol-phase processes (Zhang et al., 1994; Ravishankara,  
463 1997). The aerosol-phase processes include thermodynamically driven surface or volume-limited  
464 partitioning (including condensation for low-volatile species or solubility for volatile species) and  
465 chemically driven reactivity relevant to the functionality (Gomez et al., 2015). Ultimately, the  
466 SOA growth is dependent on the volatility of the aerosol-phase products. Evidently, there are two  
467 pathways to produce low-volatile compounds, i.e., gas-phase oxidation to yield low-volatile COOs  
468 that subsequently under condensation and multiphase reactions of volatile COOs to form low-  
469 volatile products in the aerosol-phase. In our study, the gas-to-particle conversion from *m*-xylene  
470 oxidation occurs dominantly via the latter, i.e., reactive uptake for di-carbonyls and organic acids,  
471 with a relatively small contribution from the former, i.e., condensation by low-volatile PAQs and  
472 nitrophenols. Also, our measured uptake coefficient for each COO type ( $\gamma$ ) is derived from the

473 measured particle growth (eqs. 9 and 10), which implicitly accounts for non-continuum diffusion,  
474 imperfect accommodation, and evaporation.

475 To assess the consistency of our approach, we compared the predicted and measured SOA  
476 mass yields ( $Y_{\text{SOA}}$ ), according to eq. 21. The predicted  $Y_{\text{SOA}}$  is  $(11 \pm 3)\%$  and  $(6 \pm 1)\%$ ,  
477 respectively, at 10% and 70 % RH, comparable to the measured values of  $(14 \pm 0.4)\%$  and  $(6.3 \pm$   
478  $0.2)\%$  on  $(\text{NH}_4)_2\text{SO}_4$  seed particles (Fig. 7c). The slight differences between the predicted and  
479 measured  $Y_{\text{SOA}}$ 's are explainable by the uncertainties related to lumping each COO type (i.e.,  
480 averaging the  $\gamma$  values) as well as unaccounted low-abundant COO species. To account for the  
481 RH-dependent wall loss for COOs, we corrected  $Y_{\text{SOA}}$  from the measured gaseous concentrations  
482 at varying RH (see Methods and Table S7). Such correction results in an increase of about one to  
483 four times for  $Y_{\text{SOA}}$  at 10% and 70% RH, yielding the values of  $(20 \pm 4)\%$  and  $(32 \pm 7)\%$ ,  
484 respectively (Fig. 7c). Under atmospheric conditions, SOA/BrC formation from *m*-xylene is  
485 expected to be enhanced at high RH, because of significantly enhanced aqueous reaction, larger  
486 aerosol surface-area, and higher water activity. Field measurements showed significantly enhanced  
487 SOA formation with increasing RH during severe haze evolution (Guo et al., 2014; Peng et al.,  
488 2021).

#### 489 **4. Conclusions**

490 In this work we have elucidated the production of COOs and their roles in SOA formation  
491 from *m*-xylene oxidation. The major advantages of our analytical methodologies lie in  
492 simultaneous monitoring of the evolutions of gaseous oxidation products and aerosol properties  
493 when seed particles are exposed to the oxidation products, which allows for assessment of multi-  
494 generation production of SOA and BrC. Also, our experimental approach remedies the deficiency  
495 of wall loss of reactive gaseous and particles, which represents a main obstacle in experimental

496 investigation using environmental chambers (Zhang et al., 2014; Huang et al., 2018). OH-initiated  
497 oxidation of *m*-xylene produces four distinct COO types consisting of dicarbonyls, carboxylic  
498 acids, polyhydroxy aromatics/quinones, and nitrophenols from early-generation (P<sub>2</sub> and P<sub>3</sub>), with  
499 the yields of 25%, 37%, 5%, and 3%, respectively. SOA formation occurs via several  
500 heterogeneous processes, including interfacial interaction, ionic dissociation/acid-base reaction,  
501 and oligomerization, with the yields of (20 ± 4)% at 10% RH and (32 ± 7)% at 70% RH. The  
502 identified aerosol-phase products include dominant oligomers, N-heterocycles/N-heterochains,  
503 and carboxylates at high RH and dominant carboxylates at low RH, along with small amounts of  
504 PAQ and nitrophenols (in the presence of NO<sub>x</sub>). The nitrogen-containing organics consisting of  
505 N-heterocycles, N-heterochains, and nitrophenols are light-absorbing, characterized by low SSA.  
506 The measured  $\gamma$  for COOs is dependent on the functionality, ranging from  $3.7 \times 10^{-4}$  to  $1.3 \times 10^{-2}$ .  
507 A kinetic framework is developed to predict SOA formation from the concentration and  $\gamma$  for  
508 COOs. Our results illustrate that SOA formation from *m*-xylene oxidation is accurately quantified  
509 from the abundance and reactivity for COOs (i.e., eq. 20). Notably, this kinetic framework  
510 accounts for the interfacial process (i.e., mass accommodation) as well as aqueous reactions (i.e.,  
511 oligomerization and acid-base reactions) without the assumption of gas-particle equilibrium. We  
512 envisage that this functionality-based approach is applicable to predict SOA formation from VOC  
513 photooxidation using experiment/field measured or model-simulated COOs, aerosol surface area,  
514 and reactivity. We conclude that photochemical oxidation of *m*-xylene represents a major source  
515 for SOA and BrC formation under urban conditions, because of its large abundance, high reactivity  
516 with OH, and high yields for COOs.

## 517 **ACKNOWLEDGEMENTS**



518 This research was supported by the Robert A. Welch Foundation (Grant A-1417). Y.L. was  
519 supported by a dissertation Fellowship at Texas A&M University.

## 520 REFERENCES

- 521 Atkinson, R. Atmospheric Chemistry of VOCs and NO<sub>x</sub>. *Atmos. Environ.*, 34, 2063–2101, 2000.
- 522 Calvert, J. G., Atkinson, R., Becker, K. H., Kamens, R. M., Seinfeld, J. H., Wallington, T. H., and  
523 Yarwood, G.: The Mechanisms of Atmospheric Oxidation of Aromatic Hydrocarbons, Oxford  
524 University Press: New York., 2002.
- 525 Claflin, M. S. and Ziemann, P. J.: Thermal desorption behavior of hemiacetal, acetal, ether, and  
526 ester oligomers, *Aerosol Sci. Technol.*, 53(4), 473–484, doi:10.1080/02786826.2019.1576853,  
527 2019.
- 528 Dotan, I., Albritton, D. L., Lindinger, W. and Pahl, M.: Mobilities of CO<sub>2</sub><sup>+</sup>, N<sub>2</sub>H<sup>+</sup>, H<sub>3</sub>O<sup>+</sup>,  
529 H<sub>3</sub>O<sup>+</sup>·H<sub>2</sub>O, and H<sub>3</sub>O<sup>+</sup>·(H<sub>2</sub>O)<sub>2</sub> ions in N<sub>2</sub>, *J. Chem. Phys.*, 65(11), 5028–5030,  
530 doi:10.1063/1.432943, 1976.
- 531 Fan, J., and Zhang, R.: Density Functional Theory Study on OH-Initiated Atmospheric Oxidation  
532 of m-Xylene, *J. Phys. Chem. A*, 112(18), 4314–4323, doi:10.1021/jp077648j, 2008.
- 533 Faust, J. A., Wong, J. P. S., Lee, A. K. Y., and Abbatt, J. P. D.: Role of Aerosol Liquid Water in  
534 Secondary Organic Aerosol Formation from Volatile Organic Compounds, *Environ. Sci. Technol.*,  
535 51, 1405– 1413, 2017.
- 536 Finlayson-Pitts, B. J., and Pitts, J. N.: *Chemistry of the Upper and Lower Atmosphere: Theory,*  
537 *Experiments and Applications*, Academic Press, San Diego, 2000.
- 538 Fortner, E. C., Zheng, J., Zhang, R., Berk Knighton, W., Volkamer, R. M., Sheehy, P., Molina, L.,  
539 and André, M.: Measurements of Volatile Organic Compounds Using Proton Transfer Reaction –  
540 Mass Spectrometry during the MILAGRO 2006 Campaign, *Atmos. Chem. Phys.*, 9(2), 467–481,  
541 doi:10.5194/acp-9-467-2009, 2009.
- 542 Fortner, E.C., Zhao, J., and Zhang, R.: Development of ion drift-chemical ionization mass  
543 spectrometry, *Anal. Chem.*, 76, 5436-5440, 2004.
- 544 Fountoukis, C. and Nenes, A.: SORROPIA II: A Computationally Efficient Thermodynamic  
545 Equilibrium Model for K<sup>+</sup>–Ca<sup>2+</sup>–Mg<sup>2+</sup>–NH<sub>4</sub><sup>+</sup>–Na<sup>+</sup>–SO<sub>4</sub><sup>2-</sup>–NO<sub>3</sub><sup>-</sup>–Cl–H<sub>2</sub>O Aerosols., *Atmos.*  
546 *Chem. Phys.*, 7(17), 4639–4659, doi:10.5194/acp-7-4639-2007, 2007.
- 547 Garmash, O., Rissanen, M. P., Pullinen, I., Schmitt, S., Kausiala, O., Tillmann, R., Zhao, D.,  
548 Percival, C., Bannan, T. J., Priestley, M., Hallquist, Å. M., Kleist, E., Kiendler-Scharr, A.,  
549 Hallquist, M., Berndt, T., McFiggans, G., Wildt, J., Mentel, T. F., and Ehn, M.: Multi-generation  
550 OH oxidation as a source for highly oxygenated organic molecules from aromatics, *Atmos. Chem.*  
551 *Phys.*, 20(1), 515–537, doi:10.5194/acp-20-515-2020, 2020.

552 Gomez, M.E., Lin, Y., Guo, S., and Zhang, R.: Heterogeneous chemistry of glyoxal on acidic  
553 solutions – An oligomerization pathway for secondary organic aerosol formation, *J. Phys. Chem.*,  
554 118, 4457-4463, doi:10.1021/jp509916r, 2015.

555 Guo, S., Hu, M., Zamora, M. L., Peng, J., Shang, D., Zheng, J., Du, Z., Wu, Z., Shao, M., Zeng,  
556 L., Molina, M. J., and Zhang, R.: Elucidating severe urban haze formation in China, *Proc. Natl.*  
557 *Acad. Sci. USA*, 111(49), 17373–17378, doi:10.1073/pnas.1419604111, 2014.

558 Guo, S., Hu, M., Lin, Y., Gomez-Hernandez, M., Zamora, M. L., Peng, J., Collins, D. R., and  
559 Zhang, R.: OH-Initiated Oxidation of m-Xylene on Black Carbon Aging, *Environ. Sci. Technol.*,  
560 50(16), 8605–8612, doi:10.1021/acs.est.6b01272, 2016.

561 Guo, S., Hu, M., Peng, J., Wu, Z., Zamora, M. L., Shang, D., Du, Z., Zheng, J., Fang, X., Tang,  
562 R., Wu, Y., Zeng, L., Shuai, S., Zhang, W., Wang, Y., Ji, Y., Li, Y., Zhang, A. L., Wang, W.,  
563 Zhang, F., Zhao, J., Gong, X., Wang, C., Molina, M. J. and Zhang, R.: Remarkable nucleation  
564 and growth of ultrafine particles from vehicular exhaust, *Proc. Natl. Acad. Sci.*, 117(7), 3427–  
565 3432, doi:10.1073/pnas.1916366117, 2020.

566 De Haan, D. O., Hawkins, L. N., Kononenko, J. A., Turley, J. J., Corrigan, A. L., and Tolbert, M.  
567 A., Jimenez, J. L.: Formation of Nitrogen- Containing Oligomers by Methylglyoxal and Amines  
568 in Simulated Evaporating Cloud Droplets, *Environ. Sci. Technol.*, 45, 984– 991, 2011.

569 De Haan, D. O., Hawkins, L. N., Welsh, H. G., Pednekar, R., Casar, J. R., Pennington, E. A., de  
570 Loera, A., Jimenez, N. G., Symons, M. A., Zauscher, M., Pajunoja, A., Caponi, L., Cazaunau, M.,  
571 Formenti, P., Gratien, A., Pangui, E., and Doussin, J.-F.: Brown Carbon Production in  
572 Ammonium- or Amine-Containing Aerosol Particles by Reactive Uptake of Methylglyoxal and  
573 Photolytic Cloud Cycling, *Environ. Sci. Technol.*, 51(13), 7458–7466,  
574 doi:10.1021/acs.est.7b00159, 2017.

575 Heald, C. L., Jacob, D. J., Park, R. J., Russell, L. M., Huebert, B. J., Seinfeld, J. H., Liao, H., and  
576 Weber, R. J.: A Large Organic Aerosol Source in the Free Troposphere Missing from Current  
577 Models. *Geophys. Res. Lett.*, 32, 1–4, 2005.

578 Hems, R. F., and Abbatt, J. P. D.: Aqueous Phase Photo-oxidation of Brown Carbon Nitrophenols:  
579 Reaction Kinetics, Mechanism, and Evolution of Light Absorption, *ACS Earth Sp. Chem.*, 2(3),  
580 225–234, doi:10.1021/acsearthspacechem.7b00123, 2018.

581 Hodzic, A., Kasibhatla, P. S., Jo, D. S., Cappa, C. D., Jimenez, J. L., Madronich, S., and Park, R.  
582 J.: Rethinking the Global Secondary Organic Aerosol (SOA) Budget: Stronger Production, Faster  
583 Removal, Shorter Lifetime. *Atmos. Chem. Phys.*, 16, 7917–7941, 2016.

584 Hua, W., Jubb, A. M., and Allen, H. C.: Electric Field Reversal of Na<sub>2</sub>SO<sub>4</sub>, (NH<sub>4</sub>)<sub>2</sub>SO<sub>4</sub>, and  
585 Na<sub>2</sub>CO<sub>3</sub> Relative to CaCl<sub>2</sub> and NaCl at the Air/Aqueous Interface Revealed by Heterodyne  
586 Detected Phase-Sensitive Sum Frequency, *J. Phys. Chem. Lett.*, 2(20), 2515–2520,  
587 doi:10.1021/jz200888t, 2011.

588 Huang, Y., Zhao, R., Charan, S. M., Kenseth, C. M., Zhang, X., and Seinfeld, J. H.: Unified Theory  
589 of Vapor–Wall Mass Transport in Teflon-Walled Environmental Chambers, *Environ. Sci.*  
590 *Technol.*, 52(4), 2134–2142, doi:10.1021/acs.est.7b05575, 2018.

591 Intergovernmental Panel on Climate Change (IPCC). *Climate Change 2013: The Physical Science*  
592 *Basis. Contribution of Working Group I to the Fifth Assessment Report of the Intergovernmental*  
593 *Panel on Climate Change*. Cambridge University Press, 2013.

594 Jenkin, M. E., Saunders, S. M., Wagner, V., and Pilling, M. J.: Protocol for the development of  
595 the Master Chemical Mechanism, MCM v3 (Part B): tropospheric degradation of aromatic volatile  
596 organic compounds, *Atmos. Chem. Phys.*, 3(1), 181–193, doi:10.5194/acp-3-181-2003, 2003.

597 Ji, Y., Zhao, J., Terazono, H., Misawa, K., Levitt, N. P., Li, Y., Lin, Y., Peng, J., Wang, Y., Duan,  
598 L., Pan, B., Zhang, F., Feng, X., An, T., Marrero-Ortiz, W., Secrest, J., Zhang, A. L., Shibuya, K.,  
599 Molina, M. J., and Zhang, R.: Reassessing the atmospheric oxidation mechanism of toluene, *Proc.*  
600 *Natl. Acad. Sci. USA*, 114(31), 8169–8174, doi:10.1073/pnas.1705463114, 2017.

601 Ji, Y., Shi, Q., Li, Y., An, T., Zheng, J., Peng, J., Gao, Y., Chen, J., Li, G., Wang, Y., Zhang, F.,  
602 Zhang, A. L., Zhao, J., Molina, M. J., and Zhang, R.: Carbenium ion-mediated oligomerization of  
603 methylglyoxal for secondary organic aerosol formation, *Proc. Natl. Acad. Sci. USA*, 117(24),  
604 13294 LP – 13299, doi:10.1073/pnas.1912235117, 2020.

605 Jia, L., and Xu, Y.: Effects of Relative Humidity on Ozone and Secondary Organic Aerosol  
606 Formation from the Photooxidation of Benzene and Ethylbenzene, *Aerosol Sci. Technol.*, 48(1),  
607 1–12, doi:10.1080/02786826.2013.847269, 2014.

608 Jia, L., and Xu, Y.: Different roles of water in secondary organic aerosol formation from toluene  
609 and isoprene, *Atmos. Chem. Phys.*, 18(11), 8137–8154, doi:10.5194/acp-18-8137-2018, 2018.

610 Li, G., Zhang, R., Fan, J., and Tie, X.: Impacts of biogenic emissions on photochemical ozone  
611 production in Houston, Texas, *J. Geophys. Res.*, 112, D10309, doi:10.1029/2006JD007924, 2007.

612 Li, Y., Ji, Y., Zhao, J., Wang, Y., Shi, Q., Peng, J., Wang, Y., Wang, C., Zhang, F., Wang, Y.,  
613 Seinfeld, J. H., and Zhang, R.: Unexpected Oligomerization of Small  $\alpha$ -Dicarbonyls for Secondary  
614 Organic Aerosol and Brown Carbon Formation, *Environ. Sci. Technol.*, 55(8), 4430–4439,  
615 doi:10.1021/acs.est.0c08066, 2021a.

616 Li, Y., Zhao, J., Wang, Y., Seinfeld, J. H., and Zhang, R.: Multigeneration Production of Secondary  
617 Organic Aerosol from Toluene Photooxidation, *Environ. Sci. Technol.*, 55, 8592–8603,  
618 doi:10.1021/acs.est.1c02026, 2021b.

619 Liu, J., Zhang, F., Xu, W., Sun, Y., Chen, L., Li, S., Ren, J., Hu, B., Wu, H., and Zhang, R.:  
620 Hygroscopicity of Organic Aerosols Linked to Formation Mechanisms, *Geophys. Res. Lett.*, 48(4),  
621 e2020GL091683, doi:https://doi.org/10.1029/2020GL091683, 2021.

622 Marrero-Ortiz, W., Hu, M., Du, Z., Ji, Y., Wang, Y. Y., Guo, S., Lin, Y., Gomez-Hernandez, M.,  
623 Peng, J., Li, Y., Secrest, J., Zamora, M. L., Wang, Y. Y., An, T., and Zhang, R.: Formation and

624 Optical Properties of Brown Carbon from Small  $\alpha$ -Dicarbonyls and Amines, , 53(1), 117–126,  
625 doi:10.1021/acs.est.8b03995, 2019.

626 McMurry, P. H. and Rader, D. J.: Aerosol Wall Losses in Electrically Charged Chambers, *Aerosol*  
627 *Sci. Technol.*, 4(3), 249–268, doi:10.1080/02786828508959054, 1985.

628 Molina, L. T.: Introductory lecture: air quality in megacities, *Faraday Discuss*, 226, 9-52,  
629 10.1039/d0fd00123f, 2021.

630 Moise, T., Flores, J. M., and Rudich, Y.: Optical Properties of Secondary Organic Aerosols and  
631 Their Changes by Chemical Processes, *Chem. Rev.*, 115, 4400–4439, 2015.

632 Molteni, U., Bianchi, F., Klein, F., El Haddad, I., Frege, C., Rossi, M. J., Dommen, J., and  
633 Baltensperger, U.: Formation of highly oxygenated organic molecules from aromatic compounds,  
634 *Atmos. Chem. Phys.*, 18(3), 1909–1921, doi:10.5194/acp-18-1909-2018, 2018.

635 National Academies of Sciences Engineering and Medicine (NASEM): The Future of Atmospheric  
636 Chemistry Research: Remembering Yesterday, Understanding Today, Anticipating Tomorrow,  
637 The National Academies Press, Washington, DC., 2016.

638 Ng, N. L., Kroll, J. H., Chan, A. W. H., Chhabra, P. S., Flagan, R. C., and Seinfeld, J. H.: Secondary  
639 organic aerosol formation from m-xylene, toluene, and benzene, *Atmos. Chem. Phys.*, 7(14),  
640 3909–3922, doi:10.5194/acp-7-3909-2007, 2007.

641 Nishino, N., Arey, J., and Atkinson, R.: Formation Yields of Glyoxal and Methylglyoxal from the  
642 Gas-Phase OH Radical-Initiated Reactions of Toluene, Xylenes, and Trimethylbenzenes as a  
643 Function of NO<sub>2</sub> Concentration, *J. Phys. Chem. A*, 114(37), 10140–10147,  
644 doi:10.1021/jp105112h, 2010.

645 Peng, J., Hu, M., Shang, D., Wu, Z., Du, Z., Tan, T., Wang, Y., Zhang, F., and Zhang, R.:  
646 Explosive secondary aerosol formation during severe haze in the North China Plain, *Environ. Sci.*  
647 *Technol.*, 55(4), 2189–2207, 2021.

648 Pope, C. A., III, Burnett, R. T., Thun, M. J., Calle, E. E., Krewski, D., Ito, K., and Thurston, G.  
649 D.: Lung Cancer, Cardiopulmonary Mortality, and Long-Term Exposure to Fine Particulate Air  
650 Pollution. *J. Am. Med. Assoc.*, 287, 1132–1141, 2002.

651 Qi, X., Zhu, S., Zhu, C., Hu, J., Lou, S., Xu, L., Dong, J. and Cheng, P.: Smog chamber study of  
652 the effects of NO<sub>x</sub> and NH<sub>3</sub> on the formation of secondary organic aerosols and optical properties  
653 from photo-oxidation of toluene, *Sci. Total Environ.*, 727, 138632,  
654 doi:https://doi.org/10.1016/j.scitotenv.2020.138632, 2020.

655 Ravishankara, A.R.: Heterogeneous and multiphase chemistry in the troposphere, *Science* 276,  
656 1058-1065, 1997.

657 Schwantes, R. H., Schilling, K. A., McVay, R. C., Lignell, H., Coggon, M. M., Zhang, X.,  
658 Wennberg, P. O., and Seinfeld, J. H.: Formation of highly oxygenated low-volatility products from  
659 cresol oxidation, *Atmos. Chem. Phys.*, 17(5), 3453–3474, doi:10.5194/acp-17-3453-2017, 2017.

660 Seinfeld, J. H., and Pandis, S. N.: Atmospheric chemistry and physics: from air pollution to climate  
661 change, John Wiley & Sons., 2016.

662 Shi, Q., Zhang, W., Ji, Y., Wang, J., Qin, D., Chen, J., Gao, Y., Li, G., and An, T.: Enhanced  
663 uptake of glyoxal at the acidic nanoparticle interface: implications for secondary organic aerosol  
664 formation, *Environ. Sci. Nano*, 7, 1126–1135, 2020.

665 Shrivastava, M., Cappa, C. D., Fan, J., Goldstein, A. H., Guenther, A. B., Jimenez, J. L., Kuang,  
666 C., Laskin, A., Martin, S. T., Ng, N. L., Petaja, T., Pierce, J. R., Rasch, P. J., Roldin, P., Seinfeld,  
667 J. H., Shilling, J., Smith, J. N., Thornton, J. A., Volkamer, R., Wang, J., Worsnop, D. R., Zaveri,  
668 R. A., Zelenyuk, A., and Zhang, Q.: Recent advances in understanding secondary organic aerosol:  
669 Implications for global climate forcing, *Rev. Geophys.*, 55(2), 509–559,  
670 doi:10.1002/2016RG000540, 2017.

671 Song, C., Na, K., Warren, B., Malloy, Q., and Cocker, D. R.: Secondary Organic Aerosol  
672 Formation from m-Xylene in the Absence of NO<sub>x</sub>, *Environ. Sci. Technol.*, 41(21), 7409–7416,  
673 doi:10.1021/es070429r, 2007.

674 Suh, I., Lei, W., and Zhang, R.: Experimental and theoretical studies of isoprene reaction with  
675 NO<sub>3</sub>, *J. Phys. Chem.*, 105, 6471–6478, 2001.

676 Tan, Y., Lim, Y. B., Altieri, K. E., Seitzinger, S. P., and Turpin, B. J.: Mechanisms leading to  
677 oligomers and SOA through aqueous photooxidation: insights from OH radical oxidation of acetic  
678 acid and methylglyoxal, *Atmos. Chem. Phys.*, 11, 18319–18347, 2012.

679 Wang, G., Zhang, F., Peng, J., Duan, L., Ji, Y., Marrero-Ortiz, W., Wang, J., Li, J., Wu, C., Cao,  
680 C., Wang, Y., Zheng, J., Secrest, J., Li, Y., Wang, Y., Li, H., Li, N., and Zhang, R.: Particle acidity  
681 and sulfate production during severe haze events in China cannot be reliably inferred by assuming  
682 a mixture of inorganic salts, *Atmos. Chem. Phys.*, 18, 10123–10132, doi: 10.5194/acp-18-10123-  
683 2018, 2018.

684 Wang, L., Khalizov, A. F., Zheng, J., Xu, W., Ma, Y., Lal, V. and Zhang, R.: Atmospheric  
685 nanoparticles formed from heterogeneous reactions of organics, *Nat. Geosci.*, 3(4), 238–242,  
686 doi:10.1038/ngeo778, 2010.

687 Wang, M., Chen, D., Xiao, M., Ye, Q., Stolzenburg, D., Hofbauer, V., Ye, P., Vogel, A. L.,  
688 Mauldin, R. L., Amorim, A., Baccarini, A., Baumgartner, B., Brilke, S., Dada, L., Dias, A.,  
689 Duplissy, J., Finkenzeller, H., Garmash, O., He, X.-C., Hoyle, C. R., Kim, C., Kvashnin, A.,  
690 Lehtipalo, K., Fischer, L., Molteni, U., Petäjä, T., Pospisilova, V., Quéléver, L. L. J., Rissanen, M.,  
691 Simon, M., Tauber, C., Tomé, A., Wagner, A. C., Weitz, L., Volkamer, R., Winkler, P. M., Kirkby,  
692 J., Worsnop, D. R., Kulmala, M., Baltensperger, U., Dommen, J., El-Haddad, I., and Donahue, N.  
693 M.: Photo-oxidation of Aromatic Hydrocarbons Produces Low-Volatility Organic Compounds,  
694 *Environ. Sci. Technol.*, 54(13), 7911–7921, doi:10.1021/acs.est.0c02100, 2020.

695 Wang, Y., Khalizov, A., Levy, M., and Zhang, R.: Light absorbing aerosols and their atmospheric  
696 impacts, *Atmos. Environ.*, 81, 713–715, doi:10.1016/j.atmosenv.2013.09.034, 2013.

697 Wang, Y., Lee, K.-H., Lin, Y., Levy, M., and Zhang, R.: Distinct effects of anthropogenic aerosols  
698 on tropical cyclones, *Nature Clim. Change*, 4, 368–373, doi:10.1038/nclimate2144 2014.

699 Wennberg, P. O., Bates, K. H., Crouse, J. D., Dodson, L. G., McVay, R. C., Mertens, L. A.,  
700 Nguyen, T. B., Praske, E., Schwantes, R. H., Smarte, M. D., St Clair, J. M., Teng, A. P., Zhang,  
701 X., and Seinfeld, J. H.: Gas-Phase Reactions of Isoprene and Its Major Oxidation Products, *Chem.*  
702 *Rev.*, 118, 3337–3390, 2018.

703 Xue, H., Khalizov, A. F., Wang, L., Zheng, J., and Zhang, R.: Effects of Coating of Dicarboxylic  
704 Acids on the Mass–Mobility Relationship of Soot Particles, *Environ. Sci. Technol.*, 43(8), 2787–  
705 2792, doi:10.1021/es803287v, 2009.

706 Yuan, B., Koss, A. R., Warneke, C., Coggon, M., Sekimoto, K. and de Gouw, J. A.: Proton-  
707 Transfer-Reaction Mass Spectrometry: Applications in Atmospheric Sciences, *Chem. Rev.*,  
708 117(21), 13187–13229, doi:10.1021/acs.chemrev.7b00325, 2017.

709 Zhang, D., Lei, W., and Zhang, R.: Mechanism of OH formation from ozonolysis of isoprene:  
710 Kinetics and product yields, *Chem. Phys. Lett.* 358, 171-179, 2002.

711 Zhang, F., Wang, Y., Peng, J., Chen, L., Sun, Y., Duan, L., Ge, X., Li, Y., Zhao, J., Liu, C., Zhang,  
712 X., Zhang, G., Pan, Y., Wang, Y., Zhang, A.L., Ji, Y., Wang, G., Hu, M., Molina, M.J., and Zhang,  
713 R.: An unexpected catalyst dominates formation and radiative forcing of regional haze, *Proc. Natl.*  
714 *Acad. Sci. USA*, 117, 3960-3966, doi/10.1073/pnas.1919343117, 2020.

715 Zhang, Q., Xu, Y., and Jia, L.: Secondary organic aerosol formation from OH-initiated oxidation  
716 of m-xylene: effects of relative humidity on yield and chemical composition, *Atmos. Chem. Phys.*,  
717 19(23), 15007–15021, doi:10.5194/acp-19-15007-2019, 2019.

718 Zhang, R., Leu, M.T., and Keyser, L.F.: Heterogeneous reactions involving ClONO<sub>2</sub>, HCl, and  
719 HOCl on liquid sulfuric acid surfaces, *J. Phys. Chem.*, 98, 13563-13574, 1994.

720 Zhang, R., Suh, I., Zhao, J., Zhang, D., Fortner, E. C., Tie, X., Molina, L. T. and Molina, M. J.:  
721 Atmospheric New Particle Formation Enhanced by Organic Acids, *Science* (80-. ), 304(5676),  
722 1487 LP – 1490, doi:10.1126/science.1095139, 2004.

723 Zhang, R., Wang, L., Khalizov, A. F., Zhao, J., Zheng, J., McGraw, R. L., and Molina, L. T.:  
724 Formation of nanoparticles of blue haze enhanced by anthropogenic pollution, *Proc. Natl. Acad.*  
725 *Sci. USA*, 106, doi:10.1073/pnas.0910125106, 17650-17654, 2009.

726 Zhang, R., Wang, G., Guo, S., Zamora, M. L., Ying, Q., Lin, Y., Wang, W., Hu, M., and Wang,  
727 Y.: Formation of Urban Fine Particulate Matter, *Chem. Rev.*, 115(10), 3803–3855,  
728 doi:10.1021/acs.chemrev.5b00067, 2015.

729 Zhang, R., Johnson, N.M., and Li Y.: Establishing the exposure-outcome relation between airborne  
730 particulate matter and children’s health, *Thorax*, 76, doi.org/10.1136/thoraxjnl-2021-217017, 2021.

731 Zhang, X., Cappa, C. D., Jathar, S. H., McVay, R. C., Ensberg, J. J., Kleeman, M. J., and Seinfeld,  
732 J. H.: Influence of Vapor Wall Loss in Laboratory Chambers on Yields of Secondary Organic  
733 Aerosol. *Proc. Natl. Acad. Sci. U.S.A.*, 111, 5802–5807, 2014.

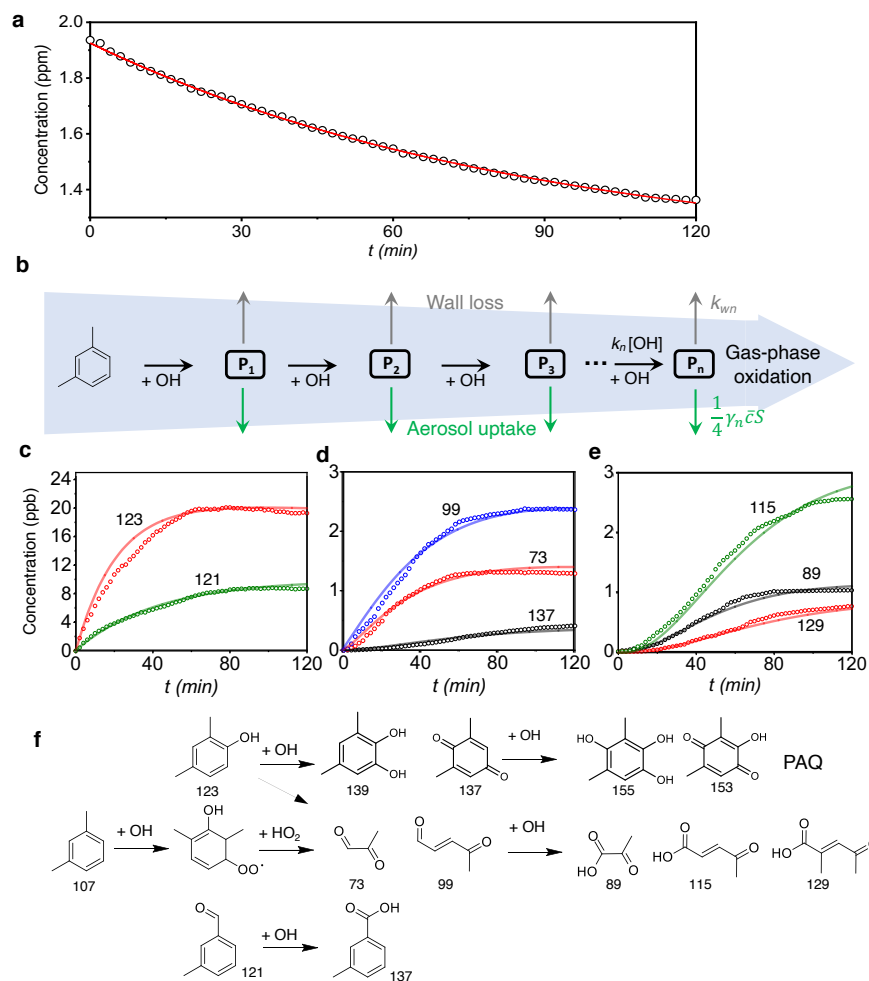
734 Zhao, J., and Zhang, R.: Proton transfer reaction rate constants between hydronium ion ( $\text{H}_3\text{O}^+$ ) and  
735 volatile organic compounds, *Atmos. Environ.*, 38(14), 2177–2185,  
736 doi:<https://doi.org/10.1016/j.atmosenv.2004.01.019>, 2004.

737 Zhao, J., Zhang, R., Fortner, E.C., and North, S.W.: Quantification of hydroxycarbonyls from OH-  
738 isoprene reactions, *J. Am. Chem. Soc.*, 126, 2686-2687, 2004.

739 Zhao, J., Zhang, R., Misawa, K., and Shibuya, K.: Experimental product study of the OH-initiated  
740 oxidation of m-xylene, *J. Photochem. Photobiol. A Chem.*, 176(1), 199–207,  
741 doi:<https://doi.org/10.1016/j.jphotochem.2005.07.013>, 2005.

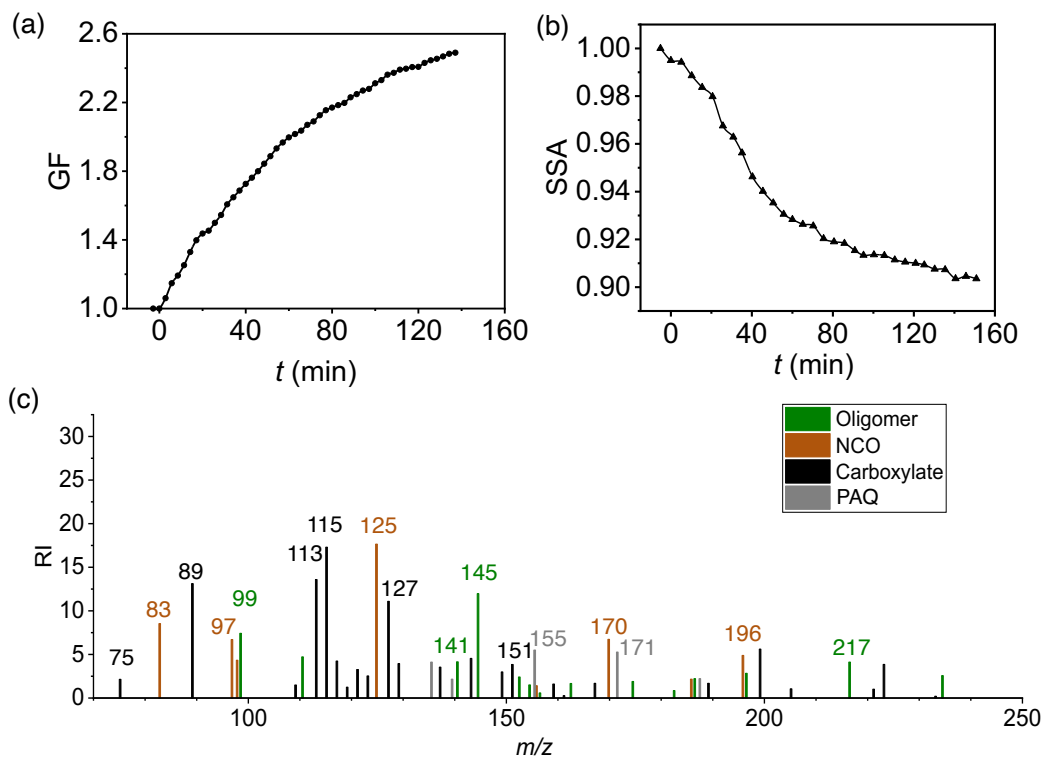
742 Zhu, J., Penner, J. E., Lin, G., Zhou, C., Xu, L., and Zhuang, B.: Mechanism of SOA formation  
743 determines magnitude of radiative effects, *P. Natl. Acad. Sci. USA*, 114, 12685–12690,  
744 <https://doi.org/10.1073/pnas.1712273114>, 2017.

745



747  
 748 **Figure 1.** OH-initiated photooxidation of *m*-xylene. (a) Time-dependent concentration of *m*-  
 749 xylene. The symbols are from the measurements, and the red solid line corresponds to exponential  
 750 fitting of the *m*-xylene concentration. The initial concentration for *m*-xylene and the estimated  
 751 steady-state concentration for OH are 1940 ppb and  $2.1 \times 10^6$  molecules  $\text{cm}^{-3}$ , respectively, with a  
 752 bimolecular rate constant of  $2.4 \times 10^{-11}$   $\text{cm}^3$  molecule $^{-1}$  s $^{-1}$ . (b) Schematic representation leading to  
 753 the multi-generation product,  $P_n$ , where  $n$  denotes the sequence of OH-initiated oxidation. The  
 754 black, gray, and green arrows denote the gas-phase oxidation, chamber wall loss, and aerosol  
 755 uptake, respectively.  $k_n$  and  $k_{wn}$  are the rate coefficients for the gas-phase oxidation and wall loss,  
 756 respectively,  $\gamma_n$  represents the aerosol uptake coefficient,  $\bar{c}$  is the thermal velocity, and  $S$  is the  
 757 aerosol surface area. (c-e) Time-dependent gas-phase concentrations of  $P_1$  (c),  $P_2$  (d), and  $P_3$  (e)  
 758 products. The symbols are from measurements, and the solid curves are simulated according to the  
 759 tri-exponential kinetics. (f) The gaseous oxidation pathways leading to the detected products. The  
 760 top row corresponds to the pathways leading to polyhydroxy aromatics/quinones (PAQ). The  
 761 numbers in (c) to (f) represents the mass to charge ratio ( $m/z$ ). All experiments are carried out for  
 762  $(\text{NH}_4)_2\text{SO}_4$  seed particles with 19 ppb  $\text{NH}_3$  at 298 K and  $\text{RH} = 70\%$ . Initiation of photooxidation  
 763 by ultraviolet light occurs at  $t = 0$ .

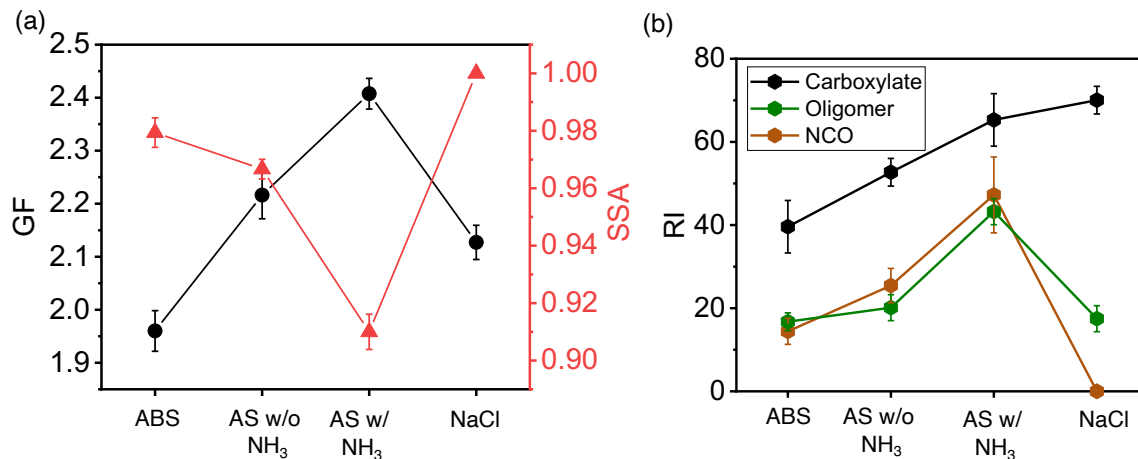




764

765 **Figure 2.** SOA and BrC formation from *m*-xylene photooxidation. Time-dependent growth factor  
 766 ( $GF = D_p/D_0$ , a) and single scattering albedo (SSA, b) of seed particles exposed to *m*-xylene  
 767 oxidation products. (c) Chemical speciation of aerosol-phase products by TD-ID-CIMS. Initiation  
 768 of photooxidation by ultraviolet light occurred at  $t = 0$ . RI denotes the relative intensity for the  
 769 integrated peak area during thermal desorption. All experiments are carried out for  $(NH_4)_2SO_4$  seed  
 770 particles with 19 ppb  $NH_3$  at 298 K and  $RH = 70\%$ .

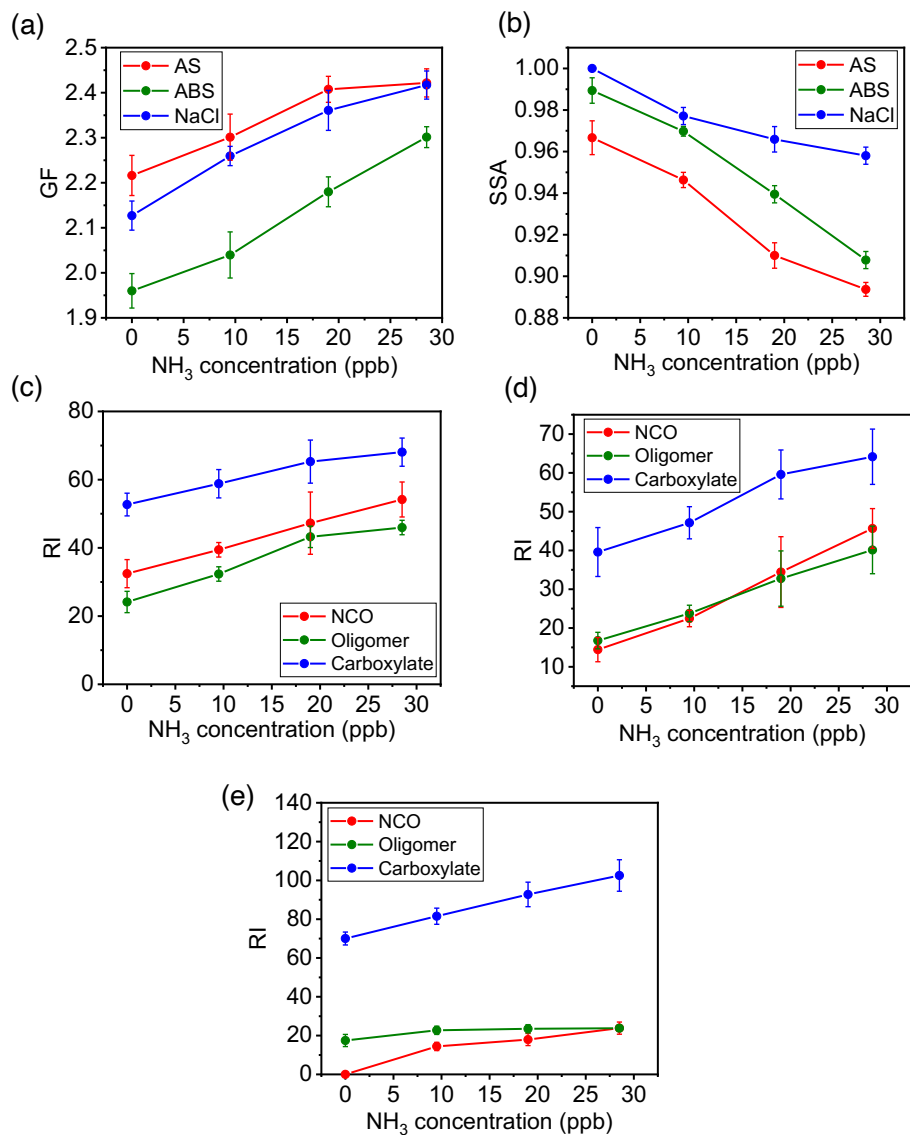
771



772

773 **Figure 3.** Dependence of SOA/BrC formation on seed particles. (a) GF (black) and SSA (red) at  
 774 120 mins of exposure for (NH<sub>4</sub>)<sub>2</sub>SO<sub>4</sub> particles in the presence (AS w/ NH<sub>3</sub>) and absence (AS w/o  
 775 NH<sub>3</sub>) of 19 ppb NH<sub>3</sub> and for NH<sub>4</sub>HSO<sub>4</sub> (ABS) and NaCl particles in the absence of NH<sub>3</sub>. (b)  
 776 Aerosol-phase relative intensity (RI) for carboxylates (black), oligomers (green), and NCO (brown)  
 777 on different seed particles. The error bar denotes 1σ of 3 replicated measurements. All particle  
 778 properties were measured relevant to dry conditions (less than 5% RH) and were dominantly  
 779 contributed by non-volatile aerosol-phase products.

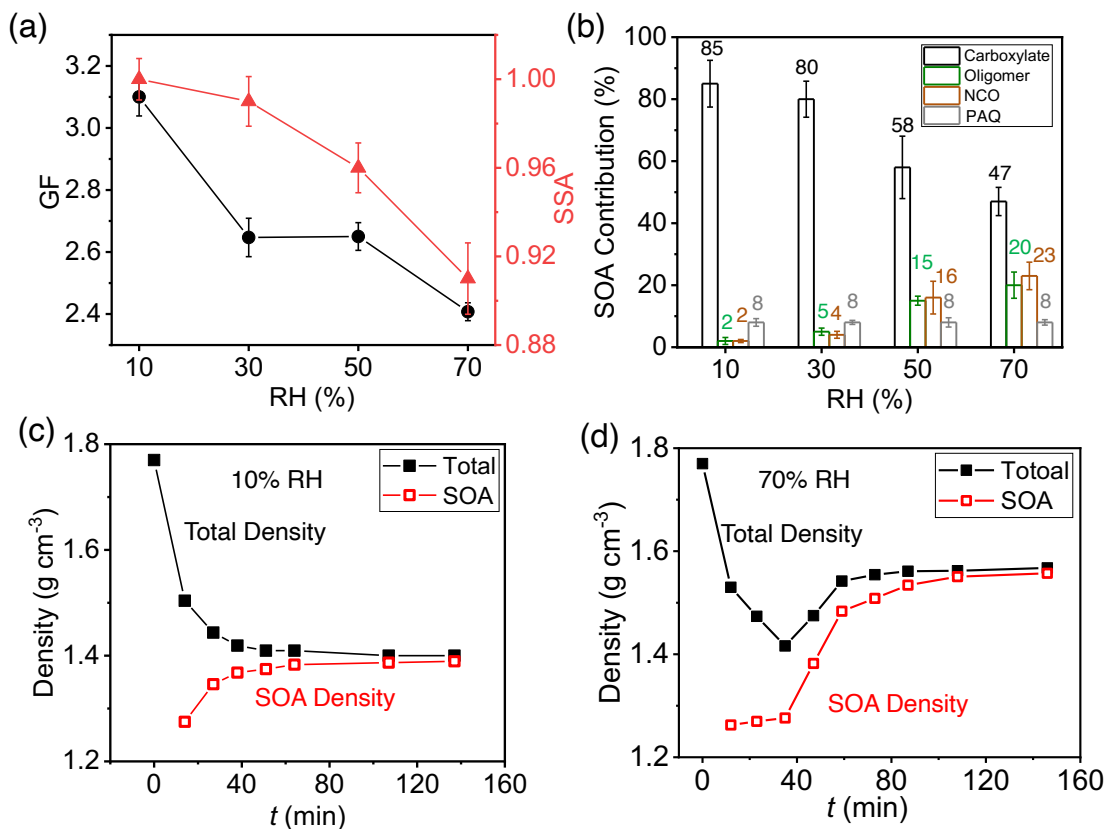
780



781

782 **Figure 4.** Variation of SOA formation with seed particles and  $\text{NH}_3$  concentration. (a,b) growth  
 783 factor (a) and SSA (b) at  $t = 120$  min with varying  $\text{NH}_3$  concentration between 0 and 27 ppb for  
 784 ammonium sulfate (AS, red), ammonium bisulfate (ABS, green), and sodium chloride (NaCl,  
 785 blue) seed particles. (c-e) Aerosol-phase mass relative intensity (RI) for NCO (red), oligomers  
 786 (green), and carboxylates (blue) on AS (c), ABS (d), and NaCl (e) seed particles. The error bar  
 787 denotes  $1\sigma$  of 3 replicated measurements.

788

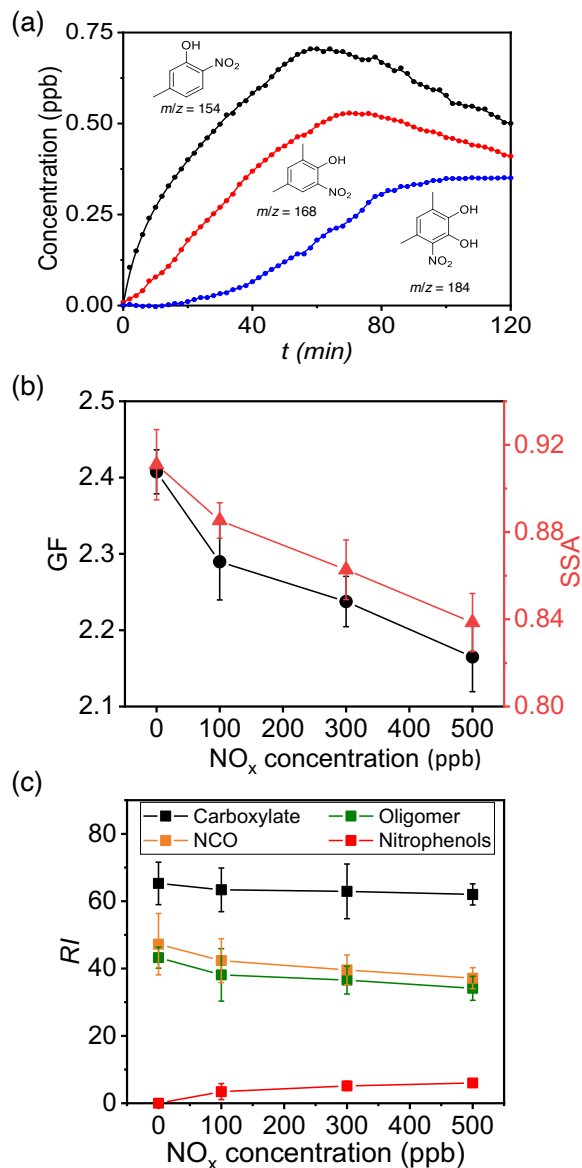


789

790 **Figure 5.** Dependence of SOA/BrC formation on RH. (a) GF (black) and SSA (red) at 120 min  
 791 with varying RH from 10% to 70%. (b) Contribution of COOs to SOA formation with varying RH  
 792 from 10% to 70%: carboxylate (black), oligomers (green), NCO (brown), and PAQ (gray) to SOA  
 793 formation. The number denotes the percentage contribution (%) of each type of aerosol-phase  
 794 products. (c,d) Time-dependent particle (black) and SOA (red) densities of seed particles exposed  
 795 to *m*-xylene oxidation products at RH = 10% (c) and 70% (d), respectively. The error bar denotes  
 796  $1\sigma$  of 3 replicated measurements.

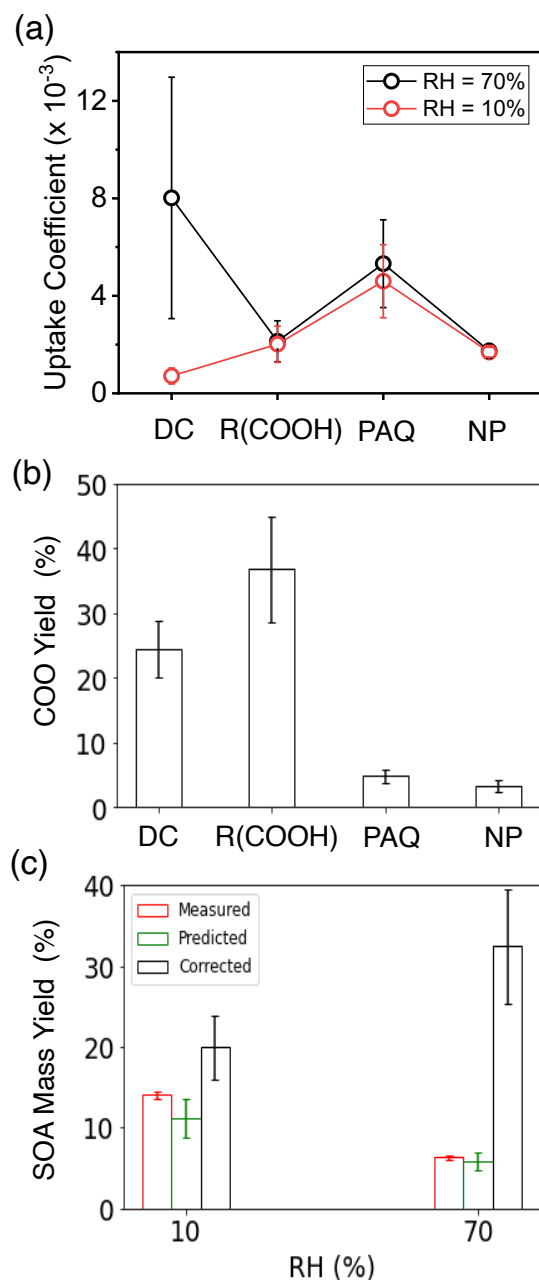
797

798



799

800 **Figure 6.** The effects of NO<sub>x</sub>. (a) Time-dependent gas-phase concentrations of 5-methyl-2-  
 801 nitrophenol (black, *m/z* = 154), dimethyl nitrophenol (red, *m/z* = 168), and dihydroxy nitrotoluene  
 802 (blue, *m/z* = 184). The numbers denote the mass to charge ratio (*m/z*). Initiation of photooxidation  
 803 by ultraviolet light occurred at *t* = 0. (b) GF (black) and SSA (red) at 120 min with varying NO<sub>x</sub>  
 804 concentration from 0 to 500 ppb. (h) Dependence of aerosol-phase relative mass intensities (RI)  
 805 for carboxylates (black), oligomers (green), NCO (brown), and nitrophenols (red) on NO<sub>x</sub>  
 806 concentration for (NH<sub>4</sub>)<sub>2</sub>SO<sub>4</sub> seed particles with 19 ppb NH<sub>3</sub> at RH = 70%. The error bar denotes  
 807 1σ of 3 replicated measurements.



808

809 **Figure 7.** Uptake coefficient, COO yield, and SOA mass yield. (a) Average uptake coefficients ( $\gamma$ )  
 810 for different types of COOs at 10% (red) and 70% (black) RH for  $(\text{NH}_4)_2\text{SO}_4$  seed particles with  
 811 19 ppb  $\text{NH}_3$  at 298 K. (b) COO yields: dicarbonyls, organic acids, polyhydroxy aromatics/quinones,  
 812 and nitrophenols are represented by DC,  $\text{R}(\text{COOH})_n$ , PAQ, and NP, respectively. (c) SOA mass  
 813 yields at 10% (left columns) and 70% RH (right). The red, green, and black columns represent the  
 814 measured, predicted, and corrected (for wall loss) SOA mass yields according to eq. 19-22. All  
 815 experiments are carried out for  $14 \mu\text{g m}^{-3}$   $(\text{NH}_4)_2\text{SO}_4$  seed particles with 19 ppb  $\text{NH}_3$  at 298 K. The  
 816 error bars denote the  $1\sigma$  of 3 replicated measurements or by accounting for error propagation of  
 817 the measured parameters.

818

819 **Table 1. Summary of experimental conditions.**

Experiment #	Seed particle	NH <sub>3</sub> concentration (ppb)	NO <sub>x</sub> concentration (ppb)	RH
Exp. 1	AS	19	0	70%
Exp. 2	AS	0	0	70%
Exp. 3	ABS	0	0	70%
Exp. 4	NaCl	0	0	70%
Exp. 5	AS	9.5	0	70%
Exp. 6	AS	28.5	0	70%
Exp. 7	ABS	9.5	0	70%
Exp. 8	ABS	19	0	70%
Exp. 9	ABS	28.5	0	70%
Exp. 10	NaCl	9.5	0	70%
Exp. 11	NaCl	19	0	70%
Exp. 12	NaCl	28.5	0	70%
Exp. 13	AS	19	0	10%
Exp. 14	AS	19	0	30%
Exp. 15	AS	19	0	50%
Exp. 16	AS	19	100	70%
Exp. 17	AS	19	300	70%
Exp. 18	AS	19	500	70%

820

821